JGR Planets

RESEARCH ARTICLE

10.1029/2020JE006693

Key Points:

- We improve approaches to quantify the spatial randomness of impact craters by applying geodesic methods
- We apply these methods to analyze the global spatial randomness of impact crater populations on Mercury, Venus, and the Moon
- We use the results to investigate known crater population variations and surface evolution scenarios on Mercury, Venus, and the Moon

Supporting Information:

- Supporting Information S1

Correspondence to:

C. Riedel,
christian.riedel@fu-berlin.de

Citation:

Riedel, C., Michael, G. G., Orgel, C., Baum, C., van der Bogert, C. H., & Hiesinger, H. (2021). Studying the global spatial randomness of impact craters on Mercury, Venus, and the Moon with geodesic neighborhood relationships. *Journal of Geophysical Research: Planets*, *126*, e2020JE006693. https://doi.org/10.1029/2020JE006693

Received 11 SEP 2020
Accepted 2 FEB 2021

Studying the Global Spatial Randomness of Impact Craters on Mercury, Venus, and the Moon With Geodesic Neighborhood Relationships

C. Riedel[1], G. G. Michael[1], C. Orgel[2], C. Baum[3], C. H. van der Bogert[4], and H. Hiesinger[4]

[1]Institute of Geological Sciences, Planetary Sciences and Remote Sensing, Freie Universität Berlin, Berlin, Germany, [2]European Space Research and Technology Centre (ESA/ESTEC), Directorate of Human and Robotic Exploration, Noordwijk, The Netherlands, [3]Department of Computer Science, Aarhus University, Aarhus, Denmark, [4]Institut für Planetologie, Westfälische Wilhelms-Universität Münster, Münster, Germany

Abstract Impact crater records on planetary surfaces are often analyzed for their spatial randomness. Generalized approaches such as the mean second closest neighbor distance (M2CND) and standard deviation of adjacent area (SDAA) are available via a software tool but do not take the influence of the planetary curvature into account in the current implementation. As a result, the measurements are affected by map distortion effects and can lead to wrong interpretations. This is particularly critical for investigations of global data sets as the level of distortion typically increases with increasing distance from the map projection center. Therefore, we present geodesic solutions to the M2CND and SDAA statistics that can be implemented in future software tools. We apply the improved methods to conduct spatial randomness analyses on global crater data sets on Mercury, Venus, and the Moon and compare the results to known crater population variations and surface evolution scenarios. On Mercury, we find that the emplacement of smooth plain deposits strongly contributed to a global clustering of craters and that a random distribution of Mercury's basins is not rejected. On Venus, the randomness analyses show that craters are largely randomly distributed across all sizes but where local nonrandom distributions due to lower crater densities in regions of recent volcanic activity may appear. On the Moon, the global clustering of craters is more pronounced than on Mercury due to mare volcanism and the Orientale impact event. Furthermore, a random distribution of lunar basins is not rejected.

Plain Language Summary The arrangement of craters on a planetary surface can be random or nonrandom. A nonrandom arrangement, such as clustered or ordered, can indicate geologic or cratering-related processes. There are generalized approaches to quantify the arrangement of craters available via a software tool. The randomness calculations in this tool rely on the spatial relationships between craters and are determined in a two-dimensional map projection. This is problematic because two-dimensional representations do not take the influence of a curved planetary surface into account. Thus, measuring the spatial arrangement of craters is prone to errors. We revise the given approaches by implementing improved computations and measure the global spatial arrangement of craters on Mercury, Venus, and the Moon. On Mercury, we observe that the smooth plains' emplacement largely causes global clustering and that the distribution of basins cannot be distinguished from a random population. On Venus, craters across all sizes are largely in a random arrangement. However, nonrandomly distributed populations may occur due to local volcanic activity. On the Moon, we observe that the emplacement of lunar maria and the Orientale impact strongly influenced the global clustering of craters. Furthermore, the arrangement of lunar basins is similar to a random distribution.

1. Introduction

Impact cratering on planetary bodies in the inner solar system occurs largely at spatially random locations. Accordingly, a significant nonrandom distribution of impact craters can indicate geologic processes that have modified the cratering record on a surface unit. Investigating whether a given crater population is either clustered, random, or in an ordered arrangement can thus provide information about the evolution of planetary surfaces. Such investigations have been used, for example, to identify possible contaminations

of the primary impactor population (e.g., Iqbal et al., 2019; Michael et al., 2012), the presence of crater saturation (e.g., Kirchoff, 2017; Squyres et al., 1997), or the nature of impactor populations (e.g., Holo & Kite, 2020).

Often, the spatial randomness of crater populations is quantified by measuring the spatial relationships between craters. Since craters are located on a curved planetary surface, the determination of such relationships requires the consideration of the planetary curvature, particularly when investigating large or global surface units. This is typically considered in individual approaches that are developed for global applications (e.g., Turcotte et al., 1999). However, two commonly applied methods that are implemented in a software tool do not consider such effects. To overcome these limitations, we use geodesic measurements that determine distances and point coordinates on a great circle and include these measurements in the referred methods. We apply the improved approaches to investigate the global spatial randomness of crater populations on Mercury, Venus, and the Moon and use the results to draw parallels to previous investigations of the surface evolution on the respective planetary bodies.

2. Quantifying the Spatial Randomness of Impact Craters

The spatial randomness of impact craters is often analyzed using Monte Carlo approaches (e.g., Hirata et al., 2020; Kreslavsky, 2007; Kirchoff, 2017; Michael et al., 2012). In such approaches, a measure that describes the population of a given set of craters is compared to the same measure of n randomly distributed crater populations, each with the same number of craters. Depending on how much the measure of the examined population deviates from the measures of the randomly distributed populations, a statement on how strongly a given set of craters differs from a random distribution can be made. The deviation from a random distribution can be quantified using statistical measures such as percentile or Z-score (e.g., Kirchoff, 2017; Michael et al., 2012; Squyres et al., 1997). The crater populations itself can in turn be described by measurements that quantify the neighborhood relationships between the craters (e.g., Kreslavsky, 2007; Michael et al., 2012; Squyres et al., 1997). This can involve the distance or the area between neighboring craters, for example.

2.1. M2CND and SDAA Statistics in the Craterstats Software

Due to the widespread use of the Craterstats software (Michael & Neukum, 2010), the mean second closest neighbor distance (M2CND) and the standard deviation of adjacent area (SDAA) (Michael et al., 2012) are widely used neighborhood relationships (e.g., Adeli et al., 2016; Hao et al., 2020; Iqbal et al., 2019; Neesemann et al., 2019) that are used to quantify the spatial randomness of impact craters. In the M2CND approach, the distance to the second closest crater centroid is determined for each crater centroid. The M2CND value results from the mean of these values. The SDAA approach is based on a Voronoi diagram that is constructed from the crater centroids. The Voronoi diagram consists of polygons in which the distance of any point to the associated crater centroid is less or the same as to any other crater centroid. The SDAA value results from the standard deviation of the area of all Voronoi polygons. In order to assess the spatial randomness of a given crater data set, the obtained measures are compared to those of randomly distributed crater data sets.

The randomness analysis in Craterstats uses two statistical measures to quantify the deviation from a random population: Percentile and Z-score (the latter is termed n_σ in the Craterstats software). The percentile marks how many percent of the randomly distributed data sets yielded a lower randomness measure than the given population. The Z-score shows the deviation from the histogram in standard deviations from the mean. A low measure in the M2CND approach indicates a clustered population (because the mean distance of second closest neighbors is smaller than for randomly distributed populations); a high measure indicates an ordered population (because the mean distance of second closest neighbors is larger than for randomly distributed populations). In the SDAA statistics, this is reversed. Here, a low measure marks an ordered population (because there is less variance in the size of Voronoi polygons compared to randomly distributed population) and a high measure marks a clustered population (because the variation in Voronoi polygon sizes is larger than for randomly distributed populations).

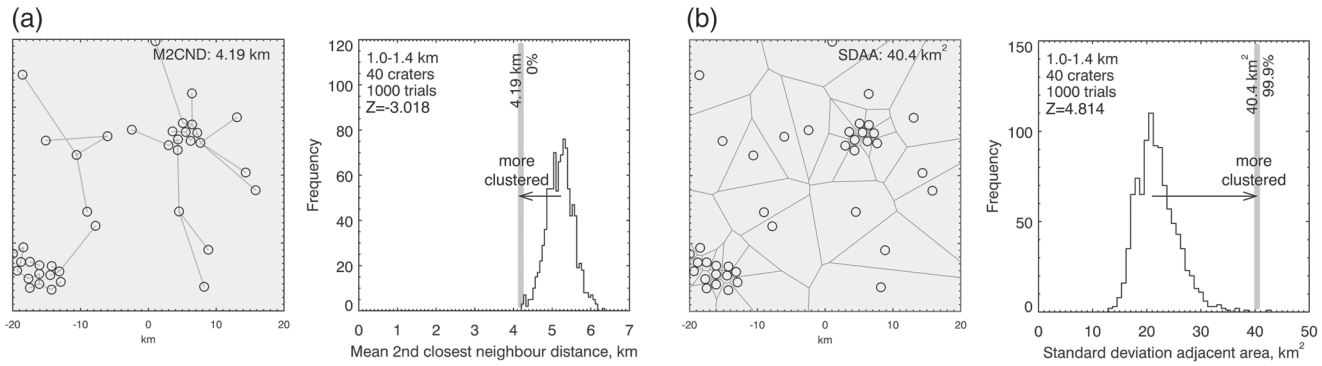

Figure 1. M2CND (Figure 1a) and SDAA statistics (Figure 1b) for a clustered set of craters. The map plots show the connecting lines between second closest neighbors that are used for the M2CND analysis (Figure 1a) and the Voronoi polygons that are used for the SDAA analysis (Figure 1b). M2CND, mean second closest neighbor distance; SDAA, standard deviation of adjacent area.

To illustrate this, we generated a clustered set of 40 same-sized craters and calculated M2CND and SDAA statistics using Craterstats. In this example, the randomness measure of the data set is compared to the randomness measures of 1,000 sets of randomly distributed craters of the same quantity. The results are shown in Figure 1. In the M2CND statistics (Figure 1a), the M2CND value of the data set is located outside the lower end of the histogram; at the 0th percentile, with a Z-score of less than -3 (more than 3σ below the mean). In the SDAA statistics (Figure 1b), the SDAA value is located at the upper end of the histogram, with a Z-score of 4.814. 99.9% of the randomly distributed crater data sets yielded a lower SDAA value than our data set. The statistical measures in both the M2CND and the SDAA statistics strongly indicate the presence of crater clusters in the given data set.

2.2. M2CND and SDAA Statistics From Geodesic Measurements

In Craterstats, all measurements as well as the construction of the Voronoi diagram are carried out in a two-dimensional Cartesian coordinate system. Accordingly, the calculated distances and areas are susceptible to map distortion effects. This affects global measurements in particular, because the distortions typically intensify with increasing distance from the map projection center (e.g., Kneissl et al, 2011; Snyder, 1987). The randomness analysis in Craterstats for example, uses measurements in the Lambert Azimuthal Equal Area (LAEA) projection, which correctly maps area sizes on a sphere, but distorts distances and shapes with increasing distance from the projection center (Snyder, 1987). We therefore apply great circle measurements to account for the curvature of planetary surfaces directly and thus circumvent the limitations of projected measurements when determining M2CND and SDAA statistics. The measurements are applied in order to (1) measure distances between craters to identify second closest neighbors for the M2CND approach and (2) determine the geodesic boundaries of Voronoi polygons for the SDAA approach.

2.2.1. M2CND

We measure the geodesic distances to all other craters for each crater in the given population, determine the neighbor with the second lowest distance for each crater and determine the M2CND value. Because a crater must have at least two adjacent craters, a minimum of three craters is required in a data set for this measurement.

2.2.2. SDAA

The calculation of global SDAA statistics requires the generation of geodesic Voronoi diagrams. For this purpose, we use the SphericalVoronoi algorithm (version 0.18.0) which is implemented in Python's scipy library (version 1.2.1) (Virtanen et al., 2020). The algorithm returns the vertices of spherical Voronoi polygons but does not generate geodesic polygon edges in the given version. In order to produce geodesic polygon edges and to construct geodesic Voronoi polygons, we use the coordinates of the polygon vertices generated by the SphericalVoronoi algorithm (we refer to these vertices as preliminary polygon vertices) and add further polygon vertices between them along a geodesic line. This ensures that the planetary curvature

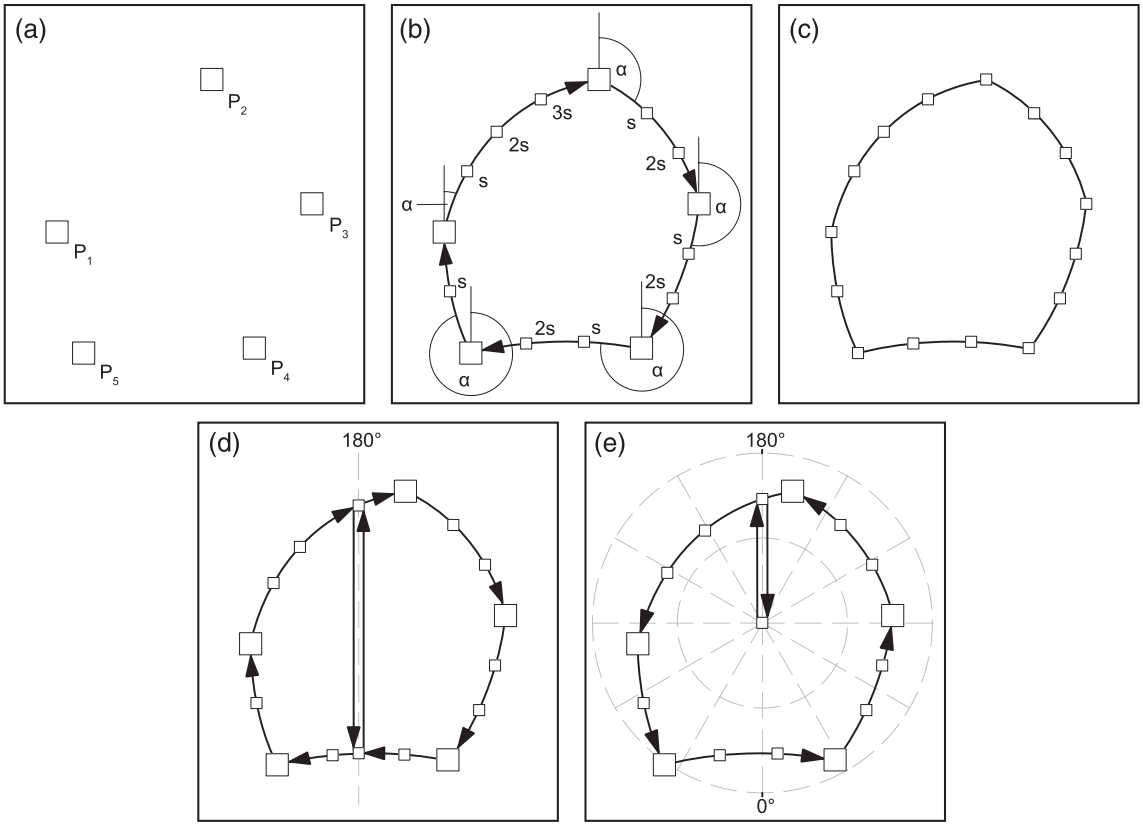

Figure 2. This figure illustrates the construction of geodesic Voronoi polygons from preliminary polygon vertices. Figure 2a shows an example of five preliminary polygon vertices P_1–P_5 as the SphericalVoronoi algorithm generates them. To create geodesic polygon edges, we calculate the coordinates of additional vertices (shown as small squares) at $s = 15$ km intervals along geodesic lines (shown as black arrows) of azimuth α (Figure 2b). The edges of the geodesic Voronoi polygon are determined from both preliminary and additional vertices (Figure 2c). In the event of a date line intersection, the date line separates the geodesic Voronoi polygon into two parts, which are constructed individually (Figure 2d). If a geodesic Voronoi polygon intersects a pole, the pole and the date line are included in the construction of the polygon (Figure 2e).

is taken into account when constructing the edges of the geodesic Voronoi polygons. We calculate the geodesic distance s between two preliminary vertices P_n and P_{n+1}. If s is larger than 15 km, we calculate the coordinates of additional vertices at fixed intervals (we use intervals of 15 km for our investigation) along a geodesic line between P_n and P_{n+1}. The geodesic Voronoi polygon is eventually constructed from both preliminary and additional vertices (see Figures 2a–2c).

If a geodesic Voronoi polygon intersects the date line or one of the poles, the construction of the polygon is slightly modified to ensure that such polygons are correctly generated. If a Voronoi polygon intersects the date line, the intersection is used as an additional vertex. In such a case, the date line acts as a cutting line, which separates the polygon into two parts. Each part is constructed individually to avoid errors when creating geodesic Voronoi polygons that cross the date line (Figure 2d). In the case of a polar intersection, we use the intersection with the date line and the pole as additional vertices and modify the order of the vertices to generate the polygon. The pole and the date line intersection form the first two and the last two vertices of the polar Voronoi polygon. All intermediate vertices are added from west to east with increasing longitude values. The polygon with its first and last vertex at the pole is thus drawn in counter-clockwise direction around the pole (Figure 2e).

When a geodesic Voronoi polygon is constructed, it is projected to the LAEA projection (centered at the corresponding crater centroid) to measure its area. The areas of all geodesic Voronoi polygons allow the determination of the SDAA value. However, a current limitation in the SphericalVoronoi algorithm allows us to only apply the approach when there is a minimum of 20 craters in the data set. A smaller number of craters can lead to incorrectly calculated polygon vertices (see Supporting Information S1 and S2).

2.3. Projected Measurements Falsify the Results of M2CND and SDAA Statistics

To illustrate how projected measurements could falsify the results of the randomness analysis, we calculate geodesic as well as Cartesian M2CND and SDAA statistics for a global data set of 100 randomly arranged craters on a sphere with lunar dimensions and compare the results. We applied the traditional crater counting technique in CSFD Tools (Riedel et al., 2018) and conducted a randomness analysis in Craterstats (Michael & Neukum, 2010; Michael et al., 2012) using Cartesian M2CND and SDAA measurements. The results are shown in Figure 3.

Due to the influence of map distortion effects, the Cartesian M2CND and SDAA values (509 km and 196,000 km^2—see Figures 3a and 3b) are different from those obtained using geodesic measurements (472.54 km and 181,000 km^2—see Figures 3c and 3d). The same applies to the calculated Z-scores and percentiles. Of 100,000 randomly distributed data sets, 88% (Cartesian M2CND, Figure 3a) and 66.9% (geodesic M2CND, Figure 3c) have lower M2CND values. This translates to Z-scores of 1.17 (Cartesian M2CND) and 0.45 (geodesic M2CND), respectively. In the SDAA analysis, 28.8% (Cartesian SDAA, Figure 3b) and 22.9% (geodesic SDAA, Figure 3d) of the randomly distributed data sets have lower SDAA values. The Z-scores are −0.59 in the Cartesian and −0.75 in the geodesic SDAA approach.

Although the differences between Cartesian and geodesic measurements in this example do not allow a reliable rejection of the random distribution, the results show that Cartesian measurements distort global M2CND and SDAA statistics. However, because it cannot be ruled out that Cartesian measurements can also lead to an incorrect assessment of the truly existing spatial randomness of impact craters, we apply geodesic measurements to calculate global M2CND and SDAA statistics for craters on Mercury, Venus, and the Moon. We apply both methods to consider the different sensitivities of the two approaches to particular crater distributions (e.g., Kreslavsky, 2007; Michael et al., 2012). In contrast to the Craterstats software, we do not apply a binning based on crater size but divide a given crater data set into overlapping bins with the same number of craters. This has several advantages: (1) the overlap allows randomness variations to be identified in a higher resolution, (2) the constant number of craters allows for a better comparison of crater populations on different planetary bodies, and (3) the constant number ensures that the randomness analysis is based on a sufficient number of craters. In our analysis, each bin contains 300 craters, with the 150 smallest craters in the next larger bin corresponding to the 150 largest craters in the next smaller bin. Due to the high number of histogram and map plots that show the results for each bin, we placed the detailed results to the Supplementary Information. A few selected histogram and map plots are included in the respective chapters.

3. The Global Spatial Randomness of Impact Craters

3.1. Mercury

3.1.1. Background

Mercury has been tectonically and volcanically active for most of its evolution (e.g., Watters et al., 2016; Zuber et al., 2012) with volcanism in particular having a major impact on its surface evolution and observable cratering record (e.g., Head et al., 2008, 2009). In its early history, the surface evolution of Mercury was dominantly shaped by effusive volcanism and global resurfacing (e.g., Byrne et al., 2016; Fassett, Kadish, et al., 2011; Marchi et al., 2013). These processes formed Mercury's most ancient surfaces on which today's observable cratering record could accumulate—the most densely cratered terrains as well as the oldest basins (e.g., Fassett et al., 2012; Marchi et al., 2013; Neukum, Oberst, et al., 2001; Orgel et al., 2020; Strom et al., 1975). These units were emplaced at around 4.0–4.1 Ga (e.g., Fassett et al., 2012; Marchi et al., 2013; Orgel et al., 2020) and are therefore a little younger than the most ancient terrains on the Moon (e.g., Orgel et al., 2018).

In the post-Late Heavy Bombardment era, volcanism continued to be an extensive process on Mercury (e.g., Head et al., 2011), but its large-scale activity declined over a relatively short period (e.g., Byrne et al., 2016; Herrick et al., 2018; Marchi et al., 2013; Wilson & Head, 2008) and ended at around 3.5 Ga (e.g., Byrne et al., 2016) due to interior cooling. The cooling led to a contraction of the planet and the appearance of tectonic features, such as thrust faults (e.g., Byrne et al., 2016; Giacomini et al., 2020; Neukum, Oberst, et al., 2001; Strom, 1977; Strom et al., 1975; Watters et al., 2009; Wilson & Head, 2008). Subsequent tectonic and volcanic activity continued to shape the surface of Mercury. However, such activity was geographically isolated (e.g.,

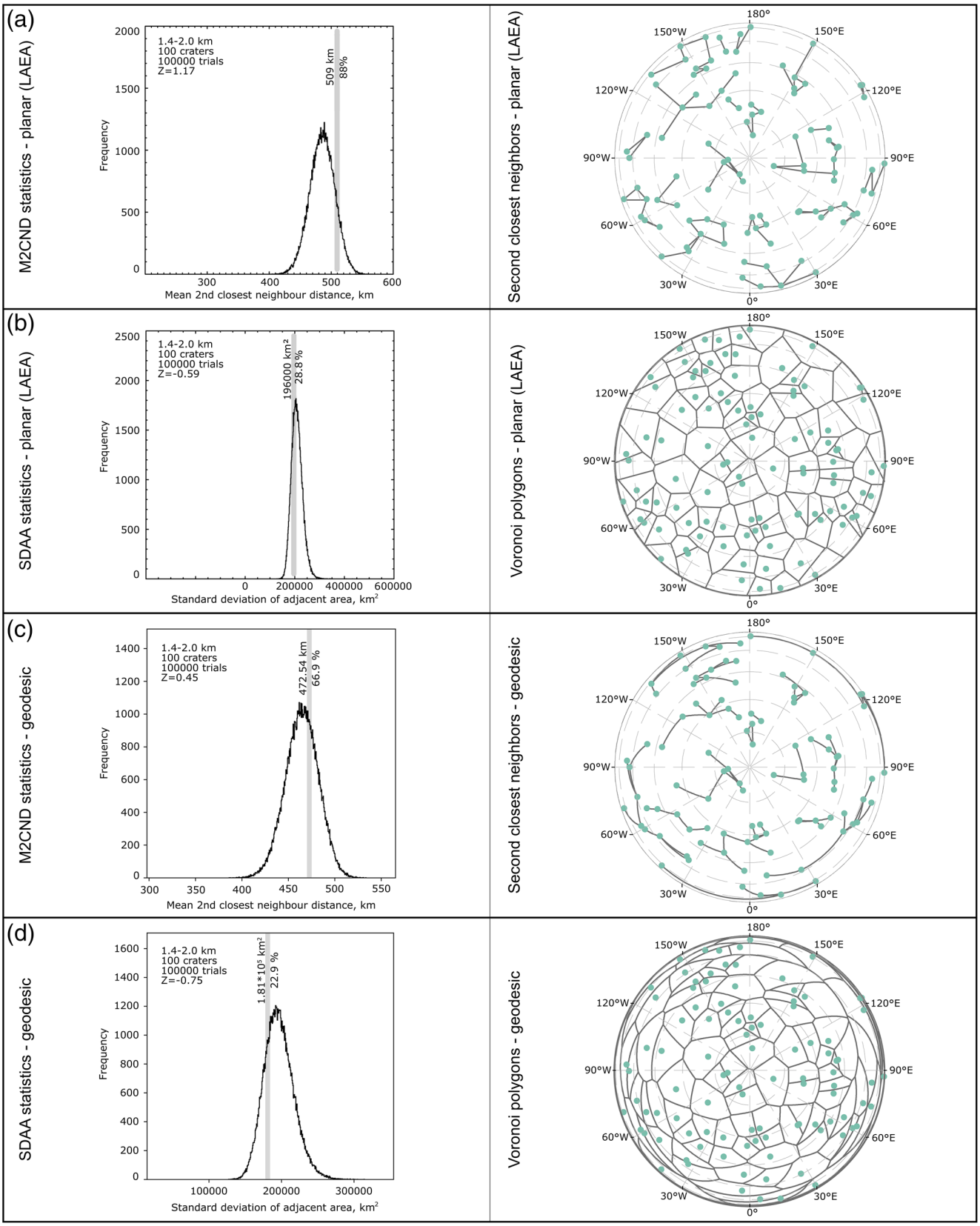
(a)
M2CND statistics - planar (LAEA)
1.4-2.0 km
100 craters
100000 trials
Z=1.17
509 km
88%
Frequency
Mean 2nd closest neighbour distance, km
Second closest neighbors - planar (LAEA)
(b)
SDAA statistics - planar (LAEA)
1.4-2.0 km
100 craters
100000 trials
Z=-0.59
196000 km²
28.8 %
Frequency
Standard deviation of adjacent area, km²
Voronoi polygons - planar (LAEA)
(c)
M2CND statistics - geodesic
1.4-2.0 km
100 craters
100000 trials
Z=0.45
472.54 km
66.9 %
Frequency
Mean 2nd closest neighbour distance, km
Second closest neighbors - geodesic
(d)
SDAA statistics - geodesic
1.4-2.0 km
100 craters
100000 trials
Z=-0.75
1.81*10⁵ km²
22.9 %
Frequency
Standard deviation of adjacent area, km²
Voronoi polygons - geodesic
180°
150°W
150°E
120°W
120°E
90°W
90°E
60°W
60°E
30°W
30°E
0°

Byrne et al., 2016; Marchi et al., 2013; Prockter et al., 2010; Thomas et al., 2014; Watters et al., 2016). Young volcanism, for example, took place primarily in the form of explosive vents (e.g., Head et al., 2009; Prockter et al., 2010; Thomas et al., 2014). Compared to the widespread flood volcanism, which dominated the surface modification of Mercury for a long time (e.g., Fassett et al., 2012; Head et al., 2009; Marchi et al., 2013), these volcanic events have little influence on the modification of Mercury's existing surface.

The geologic activities on Mercury led to the formation of two major geologic units—smooth plains and intercrater plains. The intercrater plains form the oldest terrains on Mercury and comprise areas of high crater density with interspersed smoother areas (e.g., Denevi et al., 2013; Fassett, Kadish, et al., 2011; Kreslavsky et al., 2014; Neukum, Oberst, et al., 2001; Strom et al., 1975; Strom et al., 2011). With an age of >4.0 Ga (e.g., Neukum, Oberst, et al., 2001; Strom et al., 1975), they were emplaced at a time when Mercury was volcanically very active. Although a formation as ejecta material has been debated (e.g., Wilhelms, 1976), most recent papers favor a volcanic origin of the intercrater plains (e.g., Byrne et al., 2016; Denevi et al., 2013; Strom, 1977; Strom et al., 2011). Its densely cratered landscape has a large number of secondary craters (e.g., Herrick et al., 2018; Neukum, Oberst, et al., 2001; Strom et al., 2011). However, due to strong surface modification and efficient crater degradation (e.g., Fassett et al., 2012, 2017; Fassett, Kadish, et al., 2011; Neukum, Oberst, et al., 2001), the crater densities here are lower than on the most heavily cratered terrains on the Moon (e.g., Fassett et al., 2017; Neukum, Oberst, et al., 2001; Ostrach et al., 2015).

The smooth plains, on the other hand, are younger than the intercrater plains and therefore have lower crater densities (e.g., Byrne et al., 2016; Denevi et al., 2013; Fassett, Kadish, et al., 2011; Fassett et al., 2012; Kreslavsky et al., 2014; Neukum, Oberst, et al., 2001; Ostrach et al., 2015; Strom et al., 1975; Strom et al., 2011). They are sharply demarcated from the surrounding terrain, are distributed asymmetrically, and cover roughly one third of Mercury's surface (e.g., Denevi et al., 2009, 2013). Its largest coherent units cover broad areas on the northern polar region of Mercury and around the Caloris basin (161°E; 30°N) (e.g., Denevi et al., 2013; Fassett, Kadish, et al., 2011; Fassett et al., 2012; Head et al., 2011; Neukum, Oberst, et al., 2001; Ostrach et al., 2015)—Mercury's youngest large multiring structure (e.g., Fassett et al., 2009; Neukum, Oberst, et al., 2001; Orgel et al., 2020). These northern units comprise more than half of all smooth plains (e.g., Deveni et al., 2013). Smaller smooth plain units are distributed irregularly across Mercury's surface (e.g., Byrne et al., 2016; Denevi et al., 2013; Neukum, Oberst, et al., 2001).

The majority of Mercury's smooth plains were emplaced over a relatively short period at around 3.5–3.9 Ga (e.g., Byrne et al., 2016; Denevi et al., 2013; Fassett et al., 2017; Marchi et al., 2013; Ostrach et al., 2015; Strom et al., 1975). Although there are also smaller and younger units that may have been formed by fluidized ejecta (e.g., Byrne et al., 2016; Denevi et al., 2013; Ostrach et al., 2015; Wilhelms, 1976) due to a high level of impact melt production (e.g., Ostrach et al., 2012). Overall, it is assumed that a large part of the smooth plains originated from flood volcanism (e.g., Byrne et al., 2016; Denevi et al., 2013; Head et al., 2009, 2011; Kreslavsky et al., 2014; Marchi et al., 2013; Neukum, Oberst, et al., 2001; Ostrach et al., 2015; Strom et al., 1975; Watters et al., 2009; Zuber et al., 2012), that was emplaced at various episodes (e.g., Byrne et al., 2016; Denevi et al., 2013; Neukum, Oberst, et al., 2001; Ostrach et al., 2015) and obliterated large parts of preexisting crater and basin records (Ernst et al., 2015; Fassett, Kadish, et al., 2011; Fassett et al., 2012; Head et al., 2009; Orgel et al., 2020; Ostrach et al., 2015). Such large-scale volcanic activity left most craters and basins on Mercury at least partly filled (e.g., Fassett et al., 2012; Herrick et al., 2018; Orgel et al., 2020) and strongly contributed to a lower density of craters and basins when compared to the Moon (Fassett et al., 2012; Fassett, Kadish, et al., 2011; Neukum, Oberst, et al., 2001; Orgel et al., 2020).

In this context, Fassett et al. (2012) and Orgel et al. (2020) analyzed the magnitude of basin asymmetry between Mercury's hemispheres. They found that the distribution of basins ($D \geq 300$ km) on Mercury's hemispheres is nonuniform and that the erasure of basins by resurfacing events may have contributed to it.

Figure 3. Results from Cartesian (Figures 3a and 3b) and geodesic M2CND (Figure 3c) and SDAA (Figure 3d) statistics. The histogram plots show the obtained M2CND and SDAA values of a randomly distributed set of 100 craters together with a histogram that summarizes the M2CND and SDAA values of 100,000 sets of 100 randomly distributed craters. The map plots show the Cartesian (Figure 3a) and geodesic (Figure 3c) connecting lines between second closest neighbors that are used for the M2CND analysis as well as Cartesian (Figure 3b) and geodesic Voronoi (Figure 3d) polygons that are used for the SDAA analysis. Map plots are shown in LAEA projection. LAEA, Lambert Azimuthal Equal Area; M2CND, mean second closest neighbor distance; SDAA, standard deviation of adjacent area.

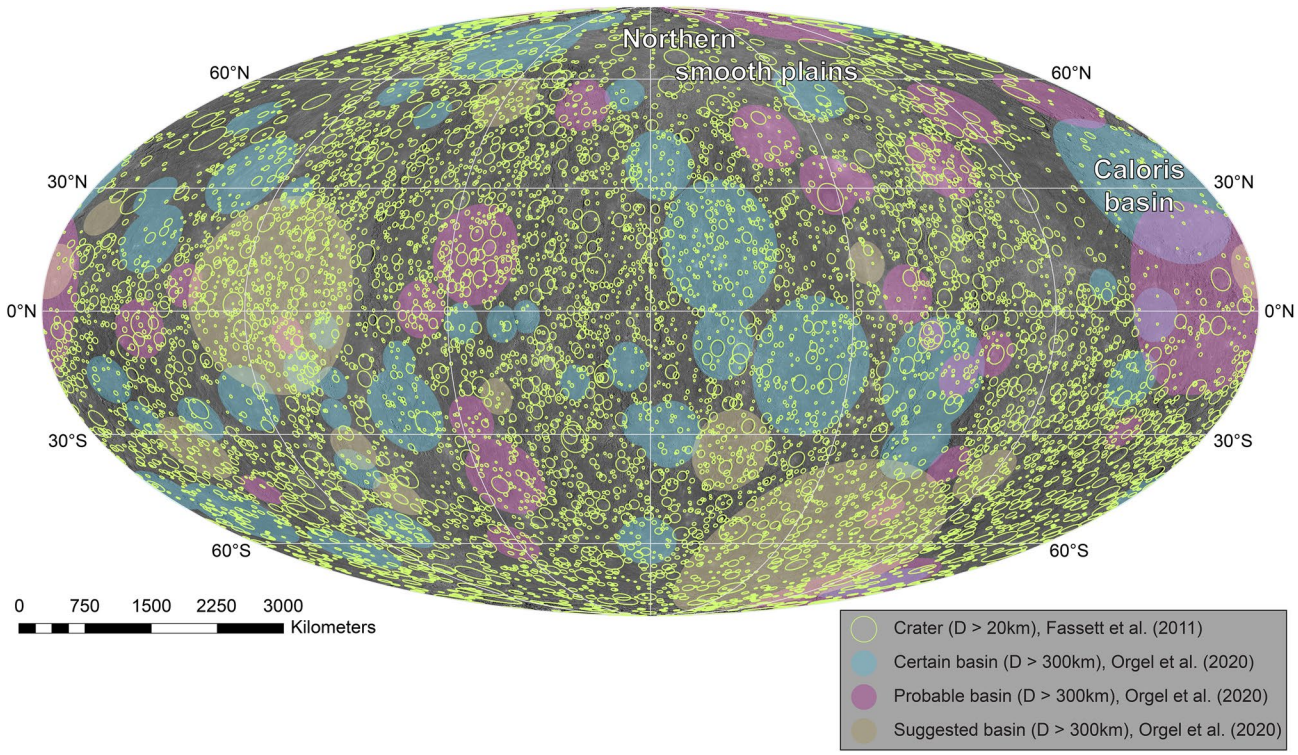

Figure 4. Map in Mollweide projection showing impact craters ($D > 20$ km) on Mercury from the data sets by Fassett et al. (2011) and Orgel et al. (2020) on a MESSENGER MDIS mosaic.

However, the studies by Fassett et al. (2012) and Orgel et al. (2020) only considered the distribution of basins over longitude. To provide more detailed information about the basin spatial relationships, we reinvestigate the global spatial randomness of impact craters and basins on Mercury by applying geodesic M2CND and SDAA analyses. To this end, we use two data sets. (1) The crater catalog by Fassett et al. (2011) (v19) to analyze the crater populations (20.36 km $\leq D <$ 300 km) and (2) the basin data set by Orgel et al. (2020) to analyze Mercury's basin populations ($D \geq$ 300 km) (Figure 4). The latter data set was created from recent investigations of Mercury's basin inventory and contains 94 basins that are labeled as "certain," "probable," and "tentative," based on their visual detectability.

3.1.2. Results

Figure 5 summarizes the results of the randomness analysis at normalized Z-scores for each bin of the crater data set by Fassett et al. (2011). The results show that the number of bins where randomness is rejected at a two-sigma confidence level is higher in the SDAA than in the M2CND analysis. Out of 47 bins, randomness is rejected in 37 (SDAA) and 14 (M2CND) populations at the given confidence level. This indicates that both approaches have a different sensitivity for the crater configurations in the given bins. Crater populations where randomness cannot be rejected at a two-sigma confidence level are more numerous in the M2CND approach and appear across all diameters in both methods. There are eight bins where a nonrandom distribution of impact craters cannot be rejected from M2CND and SDAA analyses. They occur in bins with mean diameters of 20.8, 21.2, 23.6, 24.1, 24.7, 27.1, 27.7, and 38.5 km (Figure 5 and Figures S3–S5, S8). The most significant rejection of randomness according to the SDAA analysis occurs in crater populations with 21.7 $\leq D_{\text{mean}} \leq$ 23 km (Percentiles > 99.9%, Z-scores between 3.4 and 8.9), 28.4 $\leq D_{\text{mean}} \leq$ 35.2 km (Percentiles > 98%, Z-scores between 2.2 and 6.5), and $D_{\text{mean}} \geq$ 40.9 km (Percentiles > 99.5%, Z-scores between 2.8 and 9.1). Although the significance of randomness rejection is less strong in the M2CND approach, populations where randomness is rejected at a two-sigma confidence level can be found at various size ranges as well. Therefore, the results do not expose a clear correlation between crater size and significance of nonrandomness.

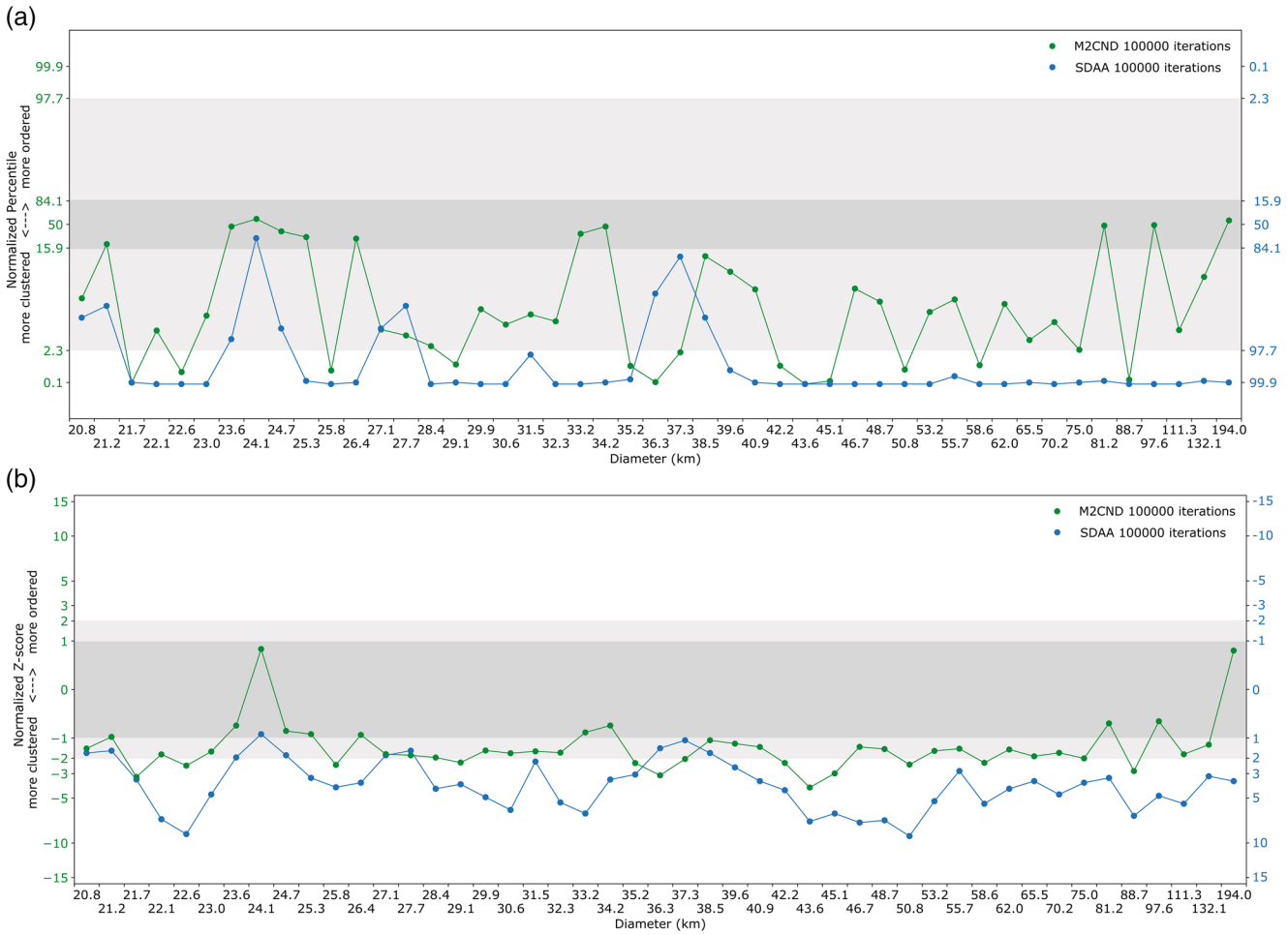

Figure 5. Normalized percentiles (Figure 5a) and *Z*-scores (Figure 5b) for binned crater data by Fassett et al. (2011), derived from geodesic M2CND and SDAA analyses. Gray bands show confidence levels at one- and two-sigma confidence levels. *X*-axis labels show the geometric mean of minimum and maximum crater diameter for each bin. M2CND, mean second closest neighbor distance; SDAA, standard deviation of adjacent area.

The map plots (Figures S3–S12) visually indicate at which geographic locations the binned crater populations occur at different densities. This allows the identification of areas in which extensive crater erasure contributed to a global-scale clustering of crater populations. Often, crater populations appear in patchy groups with extended areas of lower crater densities in between. In some bins, such as those with 23.56 km $\leq D \leq$ 24.64 km (D_{mean} = 24.1 km) or 37.37 km $\leq D \leq$ 39.62 km (D_{mean} = 38.5 km), the distribution of craters appears less grouped over the surface, which leads to a nonrejection of randomness at a two-sigma confidence level in the corresponding randomness analysis. However, because the results of the randomness analysis largely reject randomness and because crater size and the significance of randomness rejection does not correlate in our analysis, we consider this a stochastic effect rather than an indication that resurfacing did not affect the distribution of craters in the respective bins. The largest coherent areas where craters appear in a less dense configuration are located around Caloris basin and, to a lesser extent, in the northern polar region. These regions are dominated by extensive smooth plains deposits, which erased preexisting crater records. In fact, many craters in this region that are included in the crater catalog are covered by volcanic material. We therefore conclude that the emplacement of smooth plains had a significant influence on the global spatial randomness of Mercury's impact craters, where differences in surface age and crater densities cause the rejection of randomness at the given confidence level in various bins. Further small-scale resurfacing processes such as tectonics (e.g., Watters et al., 2016), the geometric overlap of preexisting craters by a new impact (sometimes referred to as cookie cutting—e.g., Kneissl et al., 2016; Richardson, 2009; Woronow, 1977), degradation from downslope diffusion (sometimes

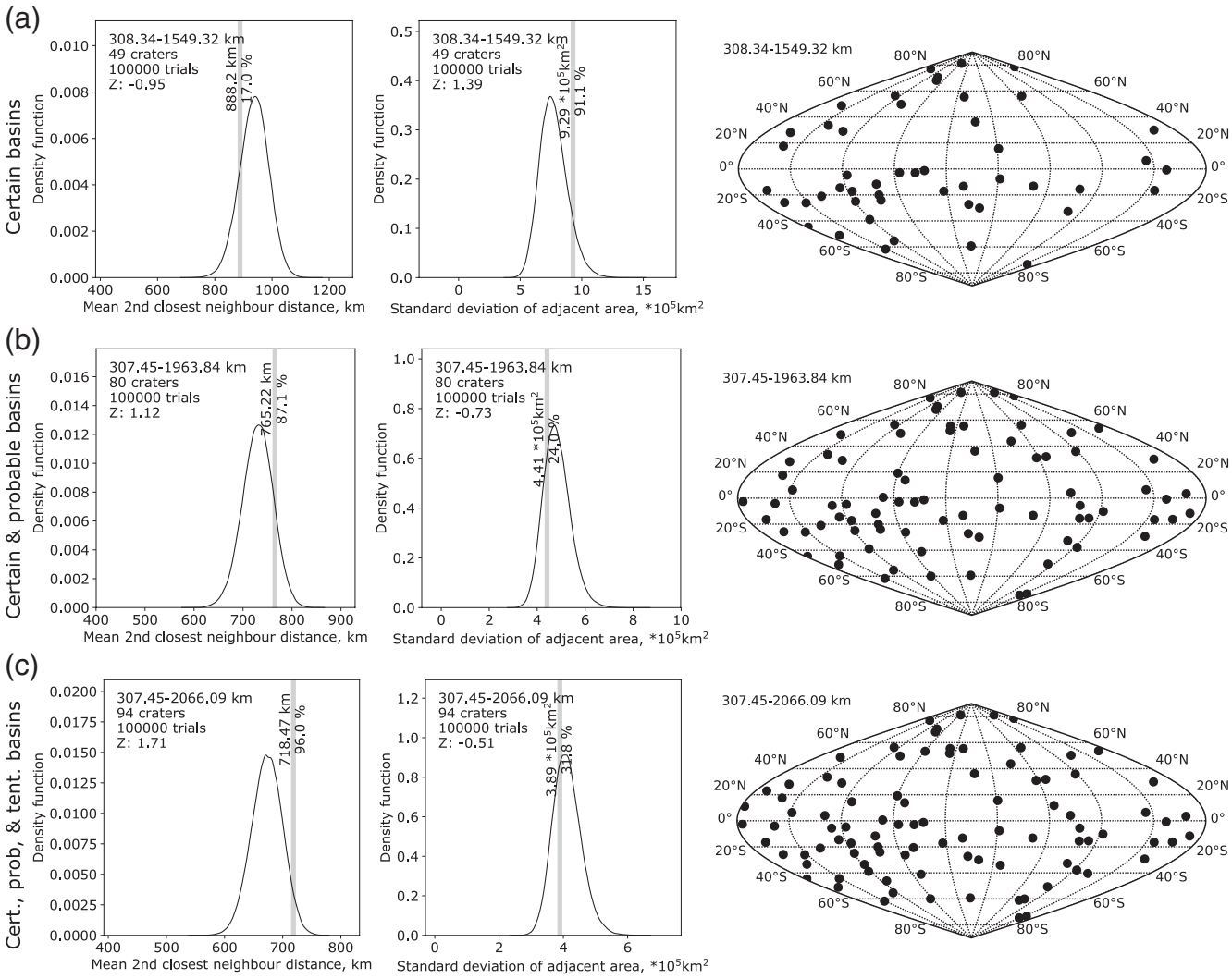

Figure 6. Histogram and map plots for certain (a), certain and probable (b), and certain, probable, and tentative basins (c) (Orgel et al., 2020). The distribution of basins is shown in sinusoidal projection.

referred to as sandblasting—e.g., Minton et al., 2019; Richardson, 2009; Soderblom, 1970), and the deposition of young smooth plains (e.g., Byrne et al., 2016) or volcanic material (e.g., Herrick et al., 2018; Thomas et al., 2014) likely contributed to the erasure of preexisting craters and the appearance of clusters in certain regions on Mercury. However, such processes occurred at a regional scale and therefore had a much smaller impact on the global clustering of impact craters.

Figure 6 shows the results from the basin data set by Orgel et al. (2020). Orgel et al. (2020) grouped basins into categories of "certain," "certain and probable," and "certain, probable, and tentative" basins and analyzed whether there is a basin asymmetry between the hemispheres on Mercury. We adopt their classification to re-analyze the distribution of Mercury's basin population. Note however, that the number of basins is much lower than the number of craters that are used to analyze the cratering record with $D < 300$ km. Therefore, the results are not directly comparable to the spatial randomness of Mercury's cratering record.

In all basin categories, randomness is not rejected at two-sigma confidence by either approach, with percentiles ranging from 17% to 96% (M2CND) as well as from 24% to 91.1% (SDAA) along with Z-scores between −0.95 and 1.71 (M2CND) as well as −0.51 and 1.39 (SDAA). Although the map plots in Figure 6 indicate that the number of basins is larger in the western than in the eastern hemisphere, as pointed out by Fassett et al. (2012) and Orgel

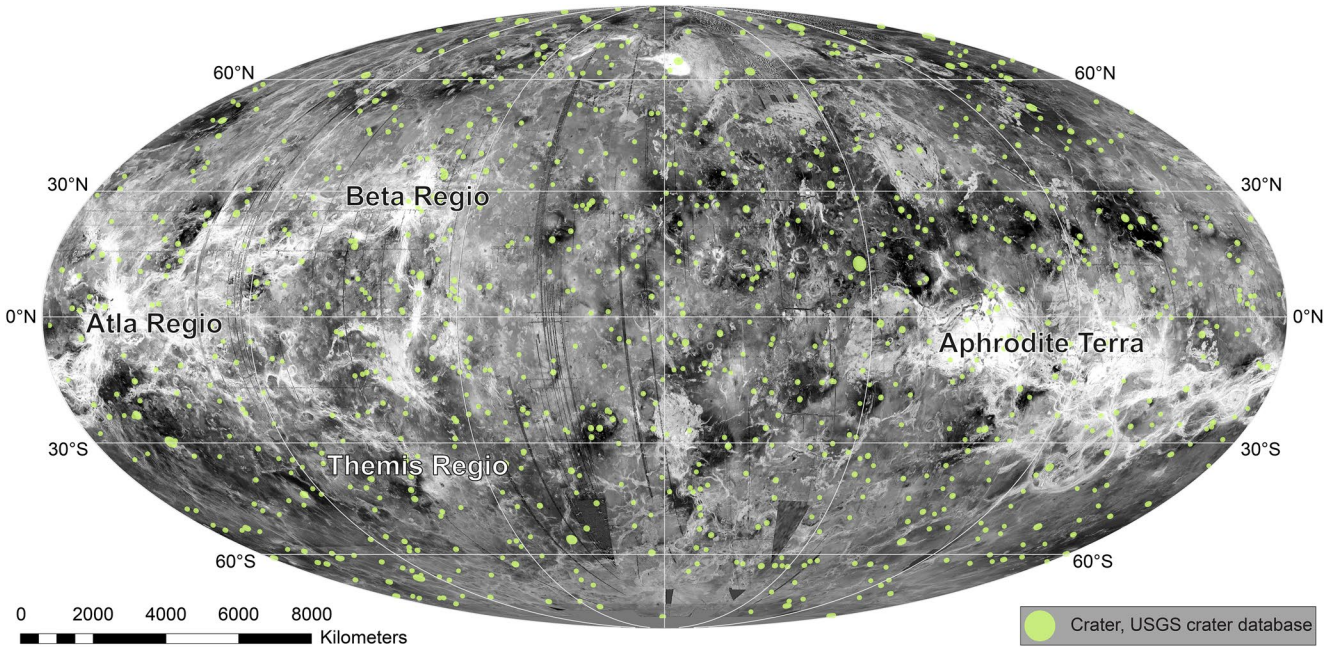

Figure 7. Map in Mollweide projection showing impact craters on Venus from the USGS Crater Database on a C3-MIDR Magellan radar mosaic.

et al. (2020), the results do not imply that such an asymmetry corresponds to a strictly nonrandom distribution of basins. Thus, the large basin distribution on Mercury could nevertheless represent a random population.

3.2. Venus

3.2.1. Background

Compared to other planetary bodies in the inner Solar System, the number of craters on Venus is low (Figure 7) with most craters showing pristine topographic features (e.g., Kreslavsky et al., 2015; Phillips et al., 1992; Schaber et al., 1992; Strom et al., 1994). Despite the presence of various geologic units that are stratigraphically different (e.g., Basilevsky & Head, 1998, 2000, 2006; Basilevsky et al., 1997; Ivanov & Head, 2011; Ivanov et al., 2015; Kreslavsky et al., 2015; Phillips et al., 1992), crater size-frequency distribution analyses have shown that there is very little variation in the spatial densities of impact craters between them (e.g., Kreslavsky et al., 2015; Schaber et al., 1992; Strom et al., 1994). This indicates that the observable surface of Venus is very young and that the visible cratering record accumulated over a recent period of probably a few hundred million years (e.g., Herrick & Rumpf, 2011; Kreslavsky et al., 2015; Phillips et al., 1992; Strom et al., 1994). Accordingly, the geologic history of Venus has strongly been influenced by resurfacing events that erased preexisting craters, mainly due to volcanic and tectonic events (e.g., Schaber et al., 1992).

There are two scenarios that describe the resurfacing history of Venus—equilibrium resurfacing and global resurfacing. In the equilibrium scenario (e.g., Bjonnes et al., 2012; Guest & Stofan, 1999; Phillips et al., 1992), volcanic and tectonic resurfacing occurred at a somewhat constant rate throughout the geologic history of Venus. This implies that the observable cratering record is related to a global crater equilibrium, where craters accumulate at the same rate they are erased. In the global resurfacing scenario (e.g., Airey et al., 2017; Basilevsky & Head, 2000, 2006; Basilevsky et al., 1997; Ivanov & Head, 2011; Ivanov et al., 2015; Kreslavsky et al., 2015; Phillips et al., 1992; Price & Suppe, 1995; Schaber et al., 1992; Strom et al., 1994), an epoch of intensive volcanism and tectonic resurfacing eliminated all craters that predate the current surface units. This was followed by an epoch of decreasing and spatially limited resurfacing activity (see e.g., Ivanov & Head, 2011) during which the observable geologic record was formed, and impact craters accumulated. Accordingly, the observable crater record on Venus largely resembles the production population and has only experienced limited volcanic and tectonic modification (e.g., Price & Suppe, 1995; Schaber et al., 1992;

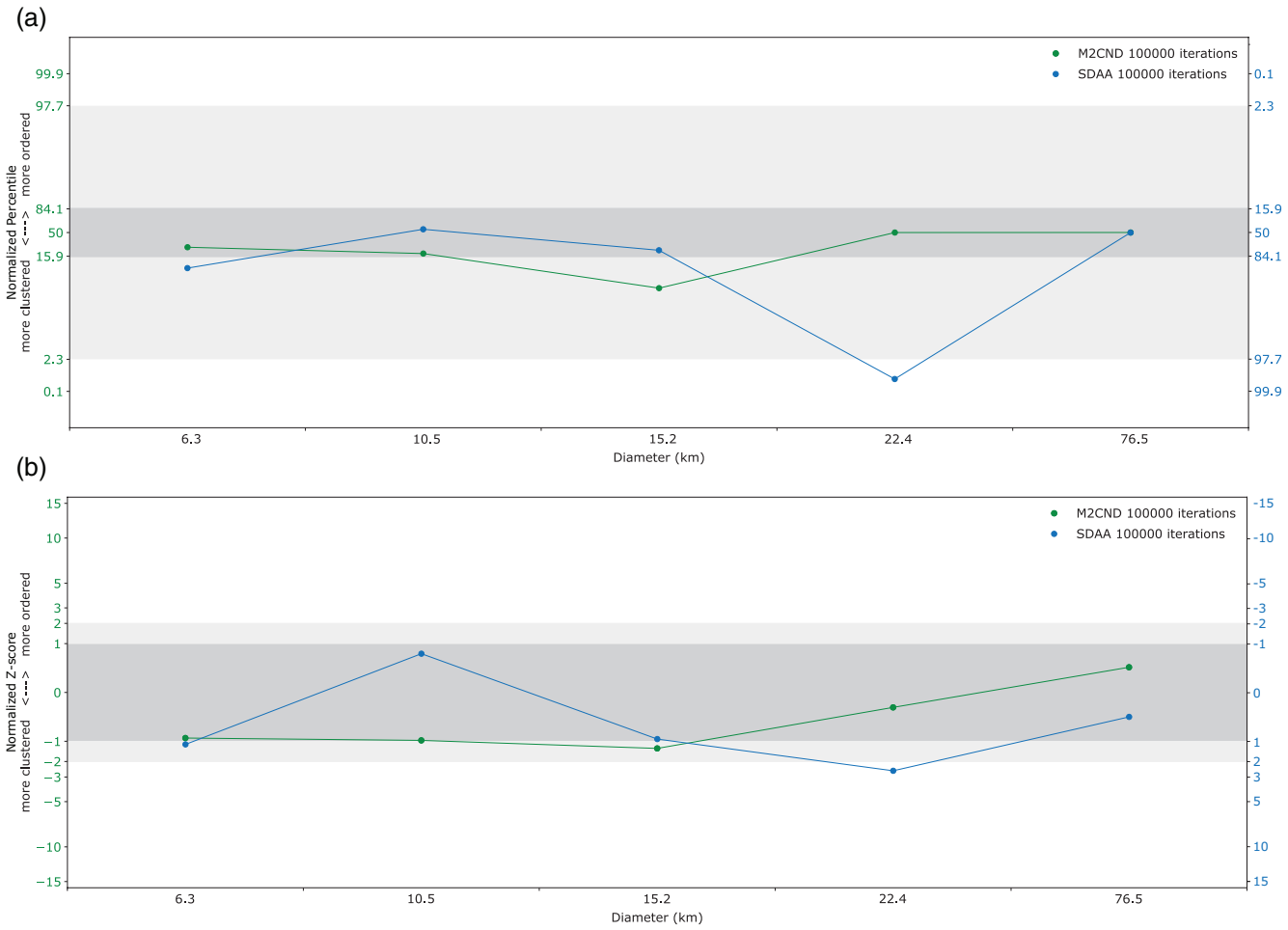

Figure 8. Normalized Percentile (a) and *Z*-score (b) for binned crater data on Venus, derived from geodesic M2CND (green) and SDAA (blue) analyses. M2CND, mean second closest neighbor distance; SDAA, standard deviation of adjacent area.

Strom et al., 1994). Due to the presence of many well-preserved impact craters (e.g., Schaber et al., 1992; Strom et al., 1994), similar crater size-frequency distributions and crater retention ages on stratigraphically different units (e.g., Kreslavsky et al., 2015; Schaber et al., 1992; Strom et al., 1994), and investigations on rift evolutions (e.g., Airey et al., 2017), most recent publications favor the global resurfacing scenario in order to describe the resurfacing history of Venus. However, this scenario is still under investigation. For example, the observations by Hauck et al. (1998) and Bjonnes et al. (2012) suggest that the equilibrium scenario cannot be excluded and that, according to Grindrod et al. (2010), Herrick and Rumpf (2011), and O'Rourke et al. (2014), the influence of volcanic and tectonic activity on crater modification may be underestimated.

In this context, the spatial randomness of impact craters was also examined and it was found that the global cratering record on Venus is randomly distributed across all crater sizes (e.g., Hauck et al., 1998; O'Rourke et al., 2014; Phillips et al., 1992; Strom et al., 1994; Turcotte et al., 1999). While Strom et al. (1994) used a chi-square test on the sine of latitude for this purpose, Phillips et al. (1992), Hauck et al. (1998), Turcotte et al. (1999), and O'Rourke et al. (2014) used a more sensitive approach based on the nearest neighbor relationships from angular distances. Here, we reinvestigate the spatial randomness of Venus' observable impact crater record based on geodesic M2CND and SDAA measurements. To this end, we use the USGS Venus Crater Database (see e.g., Schaber et al., 1992, 1995; Strom et al., 1994) with a total of 967 craters from 1.3 to 270 km in diameter.

3.2.2. Results

Figure 8 summarizes the results from the geodesic M2CND and SDAA analyses for each bin of the crater data set (for details, see Figure S13). It shows that in most cases, the crater populations cannot be distinguished

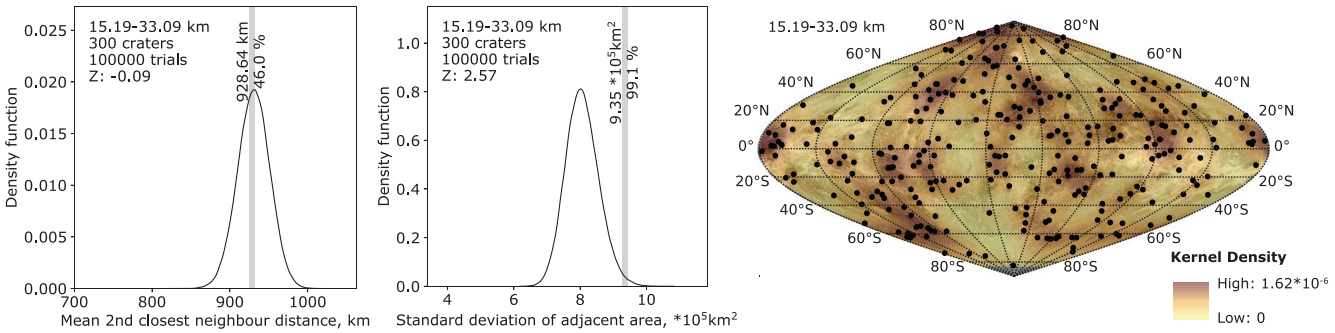

Figure 9. Results from the randomness analyses of craters with D_{mean} = 22.4 km. The map shows the distribution of craters together with crater density based on a kernel density estimation.

from a random population at two-sigma confidence. The crater population with D_{mean} = 22.4 km however, is an exception. While the M2CND analysis does not reject randomness even at a one-sigma confidence level, randomness is rejected at two-sigma confidence in the SDAA analysis. Accordingly, the SDAA approach reacts more sensitively to the different densities of impact craters in this bin than the M2CND approach. The map plot in Figure 9 indicates that areas where craters with 15.19 km ≤ D ≤ 33.09 km are somewhat less abundant are irregularly distributed across the surface. Extended areas with lower crater densities occur for example along 140°W, between 60°N and 40°S and along 20°S, between 60°E and 180°E. Although not exclusively, these areas include Aphrodite Terra area, as well as the rift zones and lobate plains of eastern Aphrodite and the Beta-Atla-Themis region. While the overall low number of small craters on Venus may be related to atmospheric filtering (e.g., Schaber et al., 1992; Strom et al., 1994) and the rejection of randomness may have a stochastic origin, the rejection of randomness in the SDAA analysis could as well be caused by local crater degradation from volcanic and tectonic events in those regions. Although recent volcanic activity on Venus is less pronounced than on Earth (e.g., Strom et al., 1994), the Beta-Atla-Themis region has been identified as an area of recent volcanic activity (e.g., Airey et al., 2017; Head et al., 1992; Schaber et al., 1992). It is therefore possible that craters have not only been modified, but also erased in these regions (e.g., Grindrod et al., 2010; Herrick & Rumpf, 2011; Strom et al., 1994), which in turn could result in a nonrandom distribution of craters with 15.19 km ≤ D ≤ 33.09 km. However, given that randomness is not rejected at two-sigma confidence in the remaining bins, this effect would be very low compared to other planetary bodies in the inner Solar System. This implies that ever since the observable cratering record accumulated on Venus, no resurfacing event was strong enough to cause significant nonrandomness of craters on a global scale. However, this does not exclude the possibility of local crater erasure by volcanic or tectonic events.

This alone however, would not necessarily reject the possibility of an equilibrium resurfacing scenario. In order to erase craters at a somewhat constant rate and to keep the global crater population spatially random, the local resurfacing events must have been efficient at degrading craters but weak at resurfacing on a global level. Still, such a scenario seems unlikely since the presence of extended areas of recent volcanic activity would contradict a random distribution of craters on Venus (e.g., Kreslavsky, 1996; Romeo, 2013; Romeo & Turcotte, 2009). Therefore, the results from the geodesic M2CND and SDAA analysis are most consistent with the global resurfacing scenario, where craters accumulated in an epoch of decreasing and spatially limited volcanic and tectonic activity (e.g., in the Beta-Atla-Themis region). In this scenario, we see a crater population that is spatially random for the most part, but where local variations in spatial crater densities due to volcanic and tectonic activity can cause a nonrandom cratering record to some extent.

3.3. Moon

3.3.1. Background

Due to the absence of an atmosphere and limited surface modification processes during its evolution, the Moon has the best preserved cratering record in the inner Solar System (Figure 10). The lunar cratering record has been used to understand the bombardment history and the planetary surface evolution on various

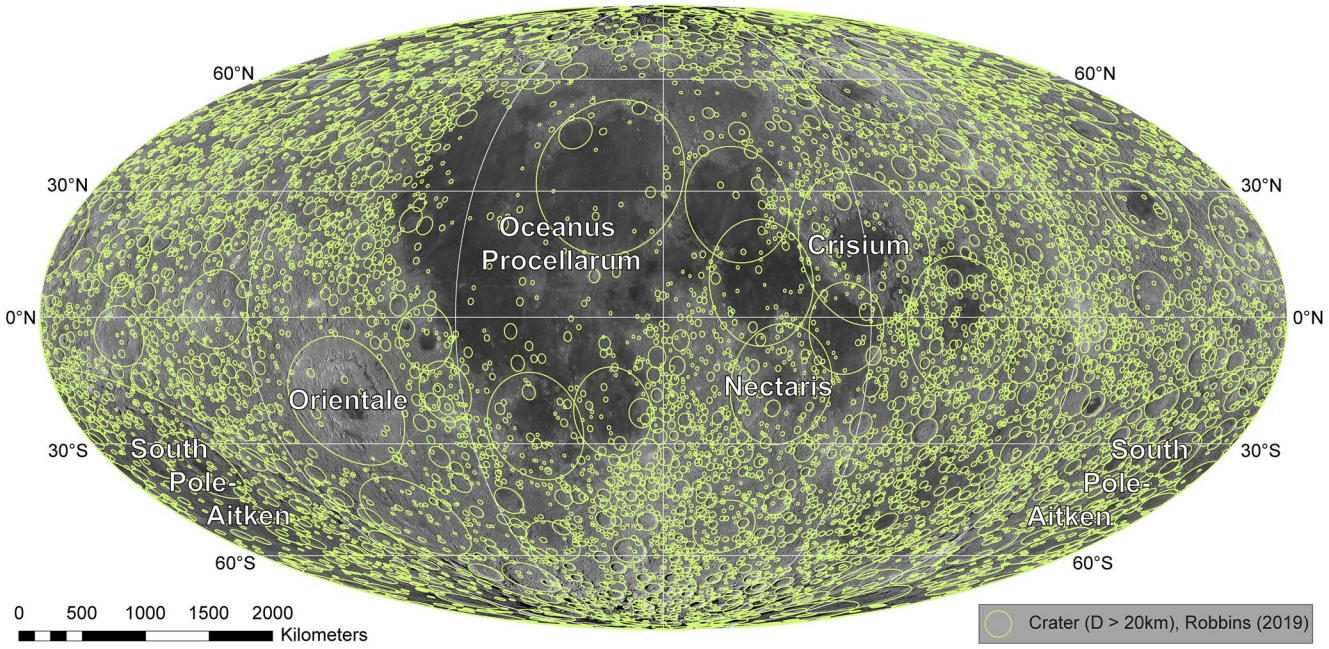

Figure 10. Map in Mollweide projection showing impact craters ($D > 20$ km) on the Moon from the Robbins (2019) data set on an LROC WAC mosaic.

other bodies in the Solar System (e.g., Fassett, 2016; Neukum, Ivanov, & Hartmann, 2001; Orgel et al., 2018; Stöffler et al., 2006; Strom et al., 2005).

Intensive bombardment and accretion of basins and craters as well as lunar volcanism have led to the formation of two major geologic units—low albedo lunar maria with smooth terrain and high albedo lunar highlands with rough terrain (e.g., Wilhelms, 1987). The lunar highlands contain the oldest lunar surface units and cover large parts of the lunar surface. They are heavily cratered, with a high density of large craters. Crater retention ages show that some lunar highland units may have surface ages of >4.3 Ga (e.g., Neukum & Ivanov, 1994; Orgel et al., 2018). The lunar maria, on the other hand, are sparsely cratered with a lower density of large craters. They are a result of flood volcanism and consist of younger surface units, which formed in topographic lows, often within old basins (e.g., Head & Wilson, 1992; Wilhelms, 1987). Lunar maria cover roughly 17% of the lunar surface (e.g., Head & Wilson, 1992), the vast majority of which is located on the lunar nearside around the Procellarum KREEP terrane (PKT). On the farside, the lunar maria are sparsely distributed and cover much smaller areas, mostly within large craters and basins. The asymmetric distribution of lunar maria has been attributed to increased volcanic activity on the lunar nearside due to a thinner crust and a higher abundance of heat producing elements (e.g., Head & Wilson, 1992; Joliff et al., 2000; Miljković et al., 2013; Wieczorek et al., 2012; Zhu et al., 2019). This in turn, resulted in higher subsurface temperatures compared to the lunar farside and the formation of larger craters and basins due to differences in target properties (Miljković et al., 2013). Crater retention ages revealed that most nearside mare were emplaced at the late stage of lunar basin formation, during the late Imbrian period, around 3.3–3.7 Ga (Hiesinger et al., 2000, 2003, 2011). Volcanic activity decreased after the late Imbrian and came to an end around 1.2 Ga, when the youngest mare units in the center of the Procellarum KREEP terrane were emplaced (Hiesinger et al., 2003). Due to the decrease in cratering rate (e.g., Neukum & Ivanov, 1994), the lunar maria are in a much more sparsely cratered state than the lunar highlands, despite their relatively long exposure to impact cratering.

With the exception of mare emplacement, geologic resurfacing and crater erasure on the Moon has largely been controlled by impact cratering processes. Cratering-related effects that contribute to the erasure of the lunar cratering record include “cookie cutting” which occurs when cratering becomes nonsparse (e.g., Kneissl et al., 2016; Minton et al., 2019; Orgel et al., 2018; Povilaitis et al., 2018; Richardson, 2009; Riedel et al., 2018; Woronow, 1977), sandblasting which contributes to topographic diffusion and simple crater equilibrium (e.g., Minton et al., 2019; Soderblom, 1970), and burial by proximal ejecta blankets (e.g.,

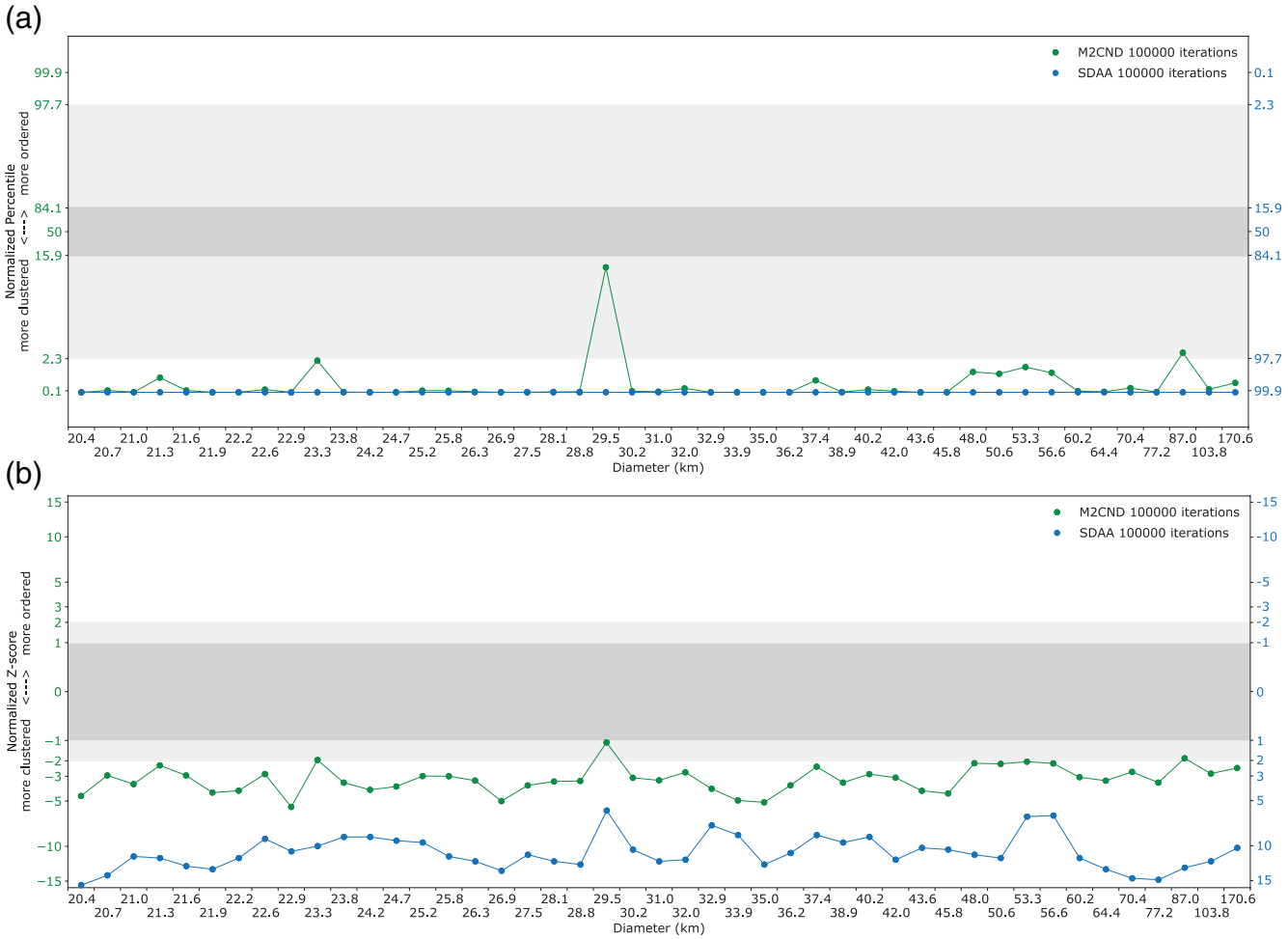

Figure 11. Normalized Percentile (a) and *Z*-score (b) for binned lunar crater data, derived from geodesic M2CND (green) and SDAA (blue) analyses. M2CND, mean second closest neighbor distance; SDAA, standard deviation of adjacent area.

Richardson, 2009). The intensity to which the individual processes influence the modification of the topography likely depends on the size of the impact (Riedel et al., 2020). Accordingly, the lunar landscape and the visible cratering record is highly influenced by crater formation and erasure. Here, we apply geodesic M2CND and SDAA statistics to investigate the global spatial randomness of lunar impact craters with $D \geq 20.08$ km. To this end, we use the lunar crater catalog by Robbins (2019) with a total of 6,973 digitized craters larger than 20 km in diameter. Smaller craters, although included in the catalog, are not taken into account in the investigation. Due to the low number of basins, we investigate the lunar cratering ($D < 300$ km) and basin record ($D \geq 300$ km) separately.

3.3.2. Results

The results from the geodesic M2CND and SDAA analyses are summarized in Figure 11 (for details, see Figures S14–S22). It shows that randomness is rejected at two-sigma confidence for nearly all binned crater populations. The significance at which randomness is rejected is stronger in the SDAA analysis, which implies that the approach reacts more sensitively to the given crater configurations than the M2CND. There are two of 45 bins where randomness is not rejected at two-sigma confidence. In bins with $D_{\text{mean}} = 29.5$ km and $D_{\text{mean}} = 87.0$ km, 13% and 2.75% of randomly distributed data sets yield a lower M2CND value than the given population, resulting in *Z*-scores of −1.13 and −1.96, respectively. However, given that the remaining binned populations as well as the SDAA analysis reject randomness at two-sigma confidence, we consider this a stochastic effect rather than an indication for a randomly distributed population.

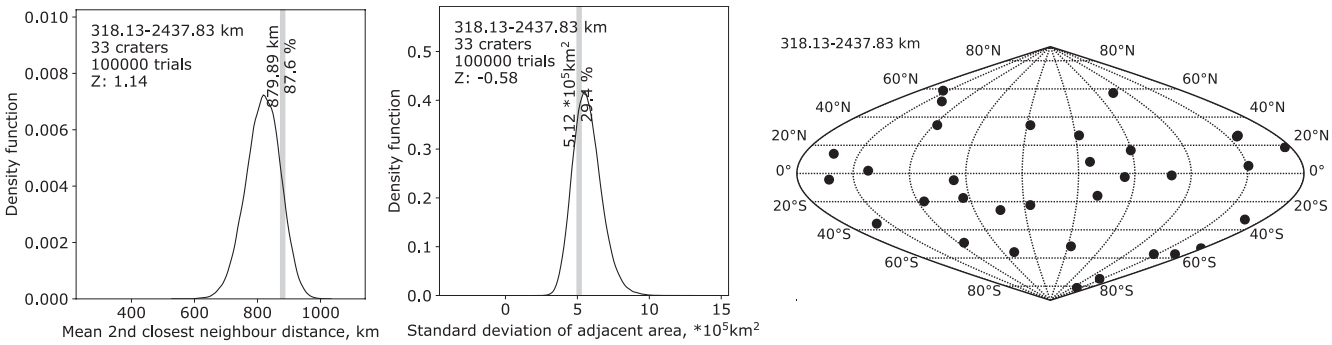

Figure 12. Histogram and map plots for lunar basins. The distribution of basins is shown in sinusoidal projection.

The results from the randomness analysis largely confirm previous investigations on lunar surface evolution and can therefore be used as an indicator that our geodesic modification of the M2CND and SDAA statistics deliver valid results. For example, the map plots (Figures S14–S22) indicate that throughout all sizes, there is a global clustering of impact craters in the binned crater populations due to differences in crater densities between ancient lunar highlands and younger surface units. These younger units involve the extended mare deposits on the lunar nearside as well as the area that surrounds Orientale basin, the youngest large basin on the Moon (e.g., Orgel et al., 2018). Accordingly, the lower density of impact craters together with a rejection of randomness confirms that a large part of preexisting craters were erased by the Orientale impact event and mare volcanism (e.g., Fassett, Head, et al., 2011; Povilaitis et al., 2018; Whitten et al., 2011).

Mare volcanism in the PKT occurred during the Imbrian, Eratosthenian, and Copernican periods, with the youngest volcanism occurring in the central PKT region (e.g., Hiesinger et al., 2003). In contrast, the mare units surrounding the center of the PKT as well as the mare areas east of it were emplaced during an earlier episode of mare volcanism, mainly during the late Imbrian period (e.g., Hiesinger et al., 2000, 2003, 2006, 2011). As a result of the different timing of mare emplacement, smaller craters with $D < 32$ km could largely accumulate in mare regions east of the PKT and around large basins, such as Crisium and Nectaris, where mare volcanism ended early, whereas ongoing mare volcanism in the central PKT contributed to a longer lasting erasure of craters, which can be seen in a low abundance of craters in all bins (Figures S14–S22). Furthermore, crater populations within the PKT are not necessarily affected by a superposing basin impact. This suggests that mare emplacement in this area could have caused the erasure of large preexisting craters larger than 100 km in diameter. Buried craters of such size have been identified by Evans et al. (2016) and Sood et al. (2017) beneath lunar mare deposits. Accordingly, lunar mare deposits in this region would have to reach thicknesses of several kilometers in order to completely cover such craters. Although the depth of lunar mare deposits is poorly constrained, various studies found evidence for a similar thickness of lunar nearside maria (e.g., Gong et al., 2016; Thomson et al., 2009; Williams & Zuber, 1998).

In contrast to the cratering record ($D < 300$ km), randomness is not rejected at two-sigma confidence for lunar basins with $D \geq 300$ km (Figure 12). The obtained M2CND value is larger than in 87.6% of the randomly distributed data sets ($Z = 1.14$) and the obtained SDAA value is larger than 29.4% of the randomly distributed data sets ($Z = -0.58$). However, since all basins are summarized in one bin, a detailed distinction between basin sizes is not possible. This implies that the nonrejection of randomness at two-sigma confidence does not necessarily contradict an asymmetry in target properties at the time of basin accretion, which influenced the final size of lunar near side and far side basins (Miljković et al., 2013). Such an investigation using M2CND and SDAA statistics would require a further subdivision of the basin population, which would involve fewer craters in the M2CND and SDAA analyses. Since involving fewer craters would yield in less representative results, M2CND and SDAA are not suitable in making such distinction from the lunar basin record. Furthermore, as the number of basins per bin is far less than 300, the results from the randomness analysis of lunar basins are not directly comparable to the spatial randomness of the lunar cratering record ($D < 300$ km).

4. Conclusions

In this study, we presented improved techniques to quantify the global spatial randomness of impact craters with respect to planetary curvature. The methods are applicable on all planetary bodies that are well approximated by a sphere. As the presented approaches are sensitive to the number of input craters, the planetary cratering records are subdivided into populations of the same quantity. Thus, it is possible to identify size-dependent variations from spatial randomness and to directly compare the spatial randomness of cratering records on different planetary bodies. The size of the subdivisions is a balance between a minimum number of craters at which variations from spatial randomness due to resurfacing events are detected and a maximum number of craters at which size-dependent variations in spatial randomness can still be identified. In our investigation, we subdivided the cratering record of the investigated bodies into bins of 300 craters to compare the results of Mercury, the Moon, and the cratering record of Venus. This number can certainly be adjusted. However, we recommend using 300 as a minimum number to properly identify nonrandom populations and to minimize stochastic effects when quantifying the spatial randomness of impact craters. We also recommend using both (or further) approaches to identify deviations from nonrandom populations since different methods can react at specific sensitivities to certain nonrandom distributions. In general, the SDAA approach showed a higher sensitivity toward nonrandom distributions in the given crater populations.

On Mercury, we identified a global clustering of impact craters with $20.36\,\text{km} \leq D < 300\,\text{km}$ due to the emplacement of extensive smooth plains deposits and the Caloris impact event. However, since the timing between the emplacement of intercrater plains and smooth plains is relatively close, the deviations from random populations are generally less significant than on the Moon. Particularly with the M2CND analysis, a random distribution of craters was not rejected at two-sigma confidence in various populations. This implies that, although major resurfacing events occurred on Mercury that cause the global cratering record with $20.36\,\text{km} \leq D < 300\,\text{km}$ to be in a clustered distribution, their influence on the global spatial randomness is less intense than on the Moon. Furthermore, the SDAA approach is more sensitive in recognizing such a resurfacing scenario. In contrast, a random distribution of basin-sized craters, was not rejected at two-sigma confidence, although previous studies indicated a basin asymmetry between Mercury's eastern and western hemisphere (Fassett et al., 2012; Orgel et al., 2020).

The randomness analyses show that craters on Venus are largely randomly distributed across all sizes. However, randomness was rejected at two-sigma confidence for the crater population with $D_{\text{mean}} = 22.4\,\text{km}$ using the SDAA approach. Although it is not clear whether the rejection of randomness is due to a stochastic effect, some of the areas where the crater density of this population is lower correspond to regions of recent volcanic activity. We therefore suggest that local volcanic activity on Venus may have contributed to crater erasure, which in turn can result in a certain nonrandom distribution of impact craters. Our results also confirm that the influence of recent volcanism on crater erasure was not strong enough to cause a significant clustering of impact craters on a global scale across all crater sizes. The given configuration could in principle be explained by an equilibrium resurfacing scenario in which the given crater configurations were caused by volcanic processes that are highly efficient at erasing craters at a local scale, but weak at resurfacing on a global level. However, such a scenario seems less likely since the geologic units in which recent volcanic modification occurred are too large to maintain a random distribution of craters (e.g., Kreslavsky, 1996; Romeo, 2013; Romeo & Turcotte, 2009). Therefore, our results are more consistent with a global resurfacing scenario, in which craters on Venus accumulated in an epoch of decreasing geologic activity and where local crater erasure in areas of recent volcanic and tectonic activity may cause the rejection of randomness in certain crater populations.

The investigation of the lunar cratering record with $20.08\,\text{km} \leq D < 300\,\text{km}$ shows that a random distribution of craters is rejected at two-sigma confidence in almost all populations, with normalized Z-scores that are clearly below the values of Mercury's crater populations in both approaches. Therefore, the global clustering of craters is more pronounced on the Moon than on Mercury. The stronger rejection of randomly distributed crater populations on the Moon is most likely caused by a greater difference in surface age between the oldest and the youngest geologic units, which leads to greater differences in crater densities. The results confirm that mare volcanism, as well as the Orientale impact event, had a major impact on the

erasure of the preexisting crater record. The results also suggest that mare emplacement in the central PKT likely caused the erasure of preexisting craters larger than 100 km in diameter. This indicates that mare deposits in this region can reach a thickness of several kilometers. In the analysis of the lunar basin record, a random distribution was not rejected at two-sigma confidence by either approach. However, this does not contradict a possible asymmetry in target properties during the time of basin emplacement (e.g., Miljković et al., 2013).

In summary, our improved methods together with a binning of crater populations allow for an accurate randomness analysis of global crater populations. The results are consistent with known population variations on Mercury, Venus, and the Moon and can be used to support a number of surface evolution scenarios on the respective planetary bodies. Therefore, we consider the presented approach to be a robust improvement to measure the spatial randomness of impact craters with respect to the planetary curvature.

Data Availability Statement

The associated data are available via Mendeley Data: Riedel et al. (2020). Studying the global spatial randomness of impact craters on Mercury, Venus, and the Moon with geodesic neighborhood relationships [Data set]. Mendeley. https://doi.org/10.17632/MN2B542K5R.2.

Acknowledgments
We thank Mikhail Kreslavsky and an anonymous reviewer for their helpful comments to improve this manuscript. We also thank Caleb Fassett for making his latest crater catalog of Mercury available to us, as well as the contributors to scipy's spherical voronoi algorithm. C. Riedel and C. Orgel were supported by German Research Foundation SFB-TRR 170, Subproject A03-126. G. G. Michael was supported by the German Aerospace Center (DLR), Grant 50QM1702. H. Hiesinger and C. H. van der Bogert were supported by DLR Project 50OW1504. Open access funding enabled and organized by Projekt DEAL.

References

Adeli, S., Hauber, E., Kleinhans, M., Le Deit, L., Platz, T., Fawdon, P., & Jaumann, R. (2016). Amazonian-aged fluvial system and associated ice-related features in Terra Cimmeria, Mars. *Icarus*, *277*, 286–299. https://doi.org/10.1016/j.icarus.2016.05.020

Airey, M. W., Mather, T. A., Pyle, D. M., & Ghail, R. C. (2017). The distribution of volcanism in the Beta-Atla-Themis region of Venus: Its relationship to rifting and implications for global tectonic regimes. *Journal of Geophysical Research: Planets*, *122*(8), 1626–1649. https://doi.org/10.1002/2016je005205

Basilevsky, A. T., & Head, J. W. (2000). Geologic units on Venus: Evidence for their global correlation. *Planetary and Space Science*, *48*(1), 75–111. https://doi.org/10.1016/s0032-0633(99)00083-5

Basilevsky, A. T., & Head, J. W. (2006). Impact craters on regional plains on Venus: Age relations with wrinkle ridges and implications for the geological evolution of Venus. *Journal of Geophysical Research*, *111*(E3). https://doi.org/10.1029/2005je002473

Basilevsky, A. T., & Head, J. W., III. (1998). The geologic history of Venus: A stratigraphic view. *Journal of Geophysical Research*, *103*(E4), 8531–8544. https://doi.org/10.1029/98je00487

Basilevsky, A. T., Head, J. W., Schaber, G. G., & Strom, R. G. (1997). The resurfacing history of Venus. In W. Bougher, D. M. Hunten, & R. J. Phillips (Eds.), *Venus II* (pp. 1047). Tucson: University of Arizona Press.

Bjonnes, E. E., Hansen, V. L., James, B., & Swenson, J. B. (2012). Equilibrium resurfacing of Venus: Results from new Monte Carlo modeling and implications for Venus surface histories. *Icarus*, *217*(2), 451–461. https://doi.org/10.1016/j.icarus.2011.03.033

Byrne, P. K., Ostrach, L. R., Fassett, C. I., Chapman, C. R., Denevi, B. W., Evans, A. J., et al. (2016). Widespread effusive volcanism on Mercury likely ended by about 3.5 Ga. *Geophysical Research Letters*, *43*(14), 7408–7416. https://doi.org/10.1002/2016gl069412

Denevi, B. W., Ernst, C. M., Meyer, H. M., Robinson, M. S., Murchie, S. L., Whitten, J. L., et al. (2013). The distribution and origin of smooth plains on Mercury. *Journal of Geophysical Research: Planets*, *118*(5), 891–907. https://doi.org/10.1002/jgre.20075

Denevi, B. W., Robinson, M., Solomon, S. C., Murchie, S. L., Blewett, D. T., Domingue, D. L., et al. (2009). The evolution of Mercury's crust: A global perspective from MESSENGER. *Science*, *324*(5927), 613–618. https://doi.org/10.1126/science.1172226

Ernst, C. M., Denevi, B. W., Barnouin, O. S., Klimczak, C., Chabot, N. L., Head, J. W., et al. (2015). Stratigraphy of the Caloris basin, Mercury: Implications for volcanic history and basin impact melt. *Icarus*, *250*, 413–429. https://doi.org/10.1016/j.icarus.2014.11.003

Evans, A. J., Soderblom, J. M., Andrews-Hanna, J. C., Solomon, S. C., & Zuber, M. T. (2016). Identification of buried lunar impact craters from GRAIL data and implications for the nearside maria. *Geophysical Research Letters*, *43*(6), 2445–2455. https://doi.org/10.1002/2015gl067394

Fassett, C. I. (2016). Analysis of impact crater populations and the geochronology of planetary surfaces in the inner solar system. *Journal of Geophysical Research: Planets*, *121*(10), 1900–1926. https://doi.org/10.1002/2016je005094

Fassett, C. I., Crowley, M. C., Leight, C., Dyar, M. D., Minton, D. A., Hirabayashi, M., et al. (2017). Evidence for rapid topographic evolution and crater degradation on Mercury from simple crater morphometry. *Geophysical Research Letters*, *44*(11), 5326–5335. https://doi.org/10.1002/2017gl073769

Fassett, C. I., Head, J. W., Baker, D. M. H., Zuber, M. T., Smith, D. E., Neumann, G. A., et al. (2012). Large impact basins on Mercury: Global distribution, characteristics, and modification history from MESSENGER orbital data. *Journal of Geophysical Research*, *117*(E12). https://doi.org/10.1029/2012je004154

Fassett, C. I., Head, J. W., Blewett, D. T., Chapman, C. R., Dickson, J. L., Murchie, S. L., et al. (2009). Caloris impact basin: Exterior geomorphology, stratigraphy, morphometry, radial sculpture, and smooth plains deposits. *Earth and Planetary Science Letters*, *285*, 297–308. https://doi.org/10.1016/j.epsl.2009.05.022

Fassett, C. I., Head, J. W., Smith, D. E., Zuber, M. T., & Neumann, G. A. (2011). Thickness of proximal ejecta from the Orientale Basin from Lunar Orbiter Laser Altimeter (LOLA) data: Implications for multi-ring basin formation. *Geophysical Research Letters*, *38*(17). https://doi.org/10.1029/2011gl048502

Fassett, C. I., Kadish, S. J., Head, J. W., Solomon, S. C., & Strom, R. G. (2011). The global population of large craters on Mercury and comparison with the Moon. *Geophysical Research Letters*, *38*(10). https://doi.org/10.1029/2011gl047294

Giacomini, L., Massironi, M., Galluzzi, V., Ferrari, S., & Palumbo, P. (2020). Dating long thrust systems on Mercury: New clues on the thermal evolution of the planet. *Geoscience Frontiers*, *11*(3), 855–870. https://doi.org/10.1016/j.gsf.2019.09.005

Gong, S., Wieczorek, M. A., Nimmo, F., Kiefer, W. S., Head, J. W., Huang, C., et al. (2016). Thicknesses of mare basalts on the Moon from gravity and topography. *Journal of Geophysical Research: Planets*, *121*(5), 854–870. https://doi.org/10.1002/2016je005008
Grindrod, P. M., Stofan, E. R., & Guest, J. E. (2010). Volcanism and resurfacing on Venus at the full resolution of Magellan SAR data. *Geophysical Research Letters*, *37*(15). https://doi.org/10.1029/2010gl043424
Guest, J. E., & Stofan, E. R. (1999). A new view of the stratigraphic history of Venus. *Icarus*, *139*(1), 55–66. https://doi.org/10.1006/icar.1999.6091
Hao, J., Michael, G. G., Adeli, S., Jaumann, R., Portyankina, G., Hauber, E., et al. (2020). Variability of spider spatial configuration at the Martian south pole. *Planetary and Space Science*, *185*, 104848. https://doi.org/10.1016/j.pss.2020.104848
Hauck, S. A., II, Phillips, R. J., & Price, M. H. (1998). Venus: Crater distribution and plains resurfacing models. *Journal of Geophysical Research*, *103*(E6), 13635–13642. https://doi.org/10.1029/98je00400
Head, J. W., Chapman, C. R., Strom, R. G., Fassett, C. I., Denevi, B. W., Blewett, D. T., et al. (2011). Flood Volcanism in the Northern High Latitudes of Mercury Revealed by MESSENGER. *Science*, *333*(6051), 1853–1856. https://doi.org/10.1126/science.1211997
Head, J. W., Crumpler, L. S., Aubele, J. C., Guest, J. E., & Saunders, R. S. (1992). Venus volcanism: Classification of volcanic features and structures, associations, and global distribution from Magellan data. *Journal of Geophysical Research*, *97*(E8), 13153. https://doi.org/10.1029/92je01273
Head, J. W., III, & Wilson, L. (1992). Lunar mare volcanism: Stratigraphy, eruption conditions, and the evolution of secondary crusts. *Geochimica et Cosmochimica Acta*, *56*(6), 2155–2175. https://doi.org/10.1016/0016-7037(92)90183-j
Head, J. W., Murchie, S. L., Prockter, L. M., Robinson, M. S., Solomon, S. C., Strom, R. G., et al. (2008). Volcanism on Mercury: Evidence from the first MESSENGER flyby. *Science*, *321*(5885), 69–72. https://doi.org/10.1126/science.1159256
Head, J. W., Murchie, S. L., Prockter, L. M., Solomon, S. C., Chapman, C. R., Strom, R. G., et al. (2009). Volcanism on Mercury: Evidence from the first MESSENGER flyby for extrusive and explosive activity and the volcanic origin of plains. *Earth and Planetary Science Letters*, *285*(3–4), 227–242. https://doi.org/10.1016/j.epsl.2009.03.007
Herrick, R. R., Bateman, E. M., Crumpacker, W. G., & Bates, D. (2018). Observations from a global database of impact craters on Mercury with diameters greater than 5 km. *Journal of Geophysical Research: Planets*, *123*(8), 2089–2109. https://doi.org/10.1029/2017je005516
Herrick, R. R., & Rumpf, M. E. (2011). Postimpact modification by volcanic or tectonic processes as the rule, not the exception, for Venusian craters. *Journal of Geophysical Research*, *116*(E2). https://doi.org/10.1029/2010je003722
Hiesinger, H., Head, J. W., III, Wolf, U., Jaumann, R., & Neukum, G. (2006). New ages for basalts in Mare Fecunditatis based on crater size-frequency measurements. *Paper presented at 37th Lunar and Planetary Science Conference, Lunar and Planetary Institute, The Woodlands, Texas, abstract #1151*.
Hiesinger, H., Head, J. W., III, Wolf, U., Jaumann, R., Neukum, G. (2011). Ages and stratigraphy of lunar mare basalts: A synthesis. *Geological Society of America Special Papers*, *477*, 1–51. https://doi.org/10.1130/2011.2477(01)
Hiesinger, H., Head, J. W., Wolf, U., Jaumann, R., & Neukum, G. (2003). Ages and stratigraphy of mare basalts in Oceanus Procellarum, Mare Nubium, Mare Cognitum, and Mare Insularum. *Journal of Geophysical Research*, *108*(E7), 5065. https://doi.org/10.1029/2002JE001985
Hiesinger, H., Jaumann, R., Neukum, G., & Head, J. W., III. (2000). Ages of mare basalts on the lunar nearside. *Journal of Geophysical Research*, *105*(E12), 29239–29275. https://doi.org/10.1029/2000je001244
Hirata, N., Morota, T., Cho, Y., Kanamaru, M., Watanabe, S., Sugita, S., et al. (2020). The spatial distribution of impact craters on Ryugu. *Icarus*, *338*, 113527. https://doi.org/10.1016/j.icarus.2019.113527
Holo, S., & Kite, E. (2020). The spatial signature of a changing ancient impactor population for Mars. *Icarus*, *337*, 113447. https://doi.org/10.1016/j.icarus.2019.113447
Iqbal, W., Hiesinger, H., & van der Bogert, C. H. (2019). Geological mapping and chronology of lunar landing sites: Apollo 11. *Icarus*, *333*, 528–547. https://doi.org/10.1016/j.icarus.2019.06.020
Ivanov, M. A., & Head, J. W. (2011). Global geological map of Venus. *Planetary and Space Science*, *59*(13), 1559–1600. https://doi.org/10.1016/j.pss.2011.07.008
Ivanov, M. A., Head, J. W., & Basilevsky, A. T. (2015). History of the long-wavelength topography of Venus. *Solar System Research*, *49*(1), 1–11. https://doi.org/10.1134/s0038094615010025
Jolliff, B. L., Gillis, J. J., Haskin, L. A., Korotev, R. L., & Wieczorek, M. A. (2000). Major lunar crustal terranes: Surface expressions and crust-mantle origins. *Journal of Geophysical Research*, *105*(E2), 4197–4216. https://doi.org/10.1029/1999je001103
Kirchoff, M. R. (2017). Can spatial statistics help decipher impact crater saturation? *Meteoritics & Planetary Sciences*, *53*(4), 874–890. https://doi.org/10.1111/maps.13014
Kneissl, T., Michael, G. G., & Schmedemann, N. (2016). Treatment of non-sparse cratering in planetary surface dating. *Icarus*, *277*, 187–195. https://doi.org/10.1016/j.icarus.2016.05.015
Kneissl, T., van Gasselt, S., & Neukum, G. (2011). Map-projection-independent crater size-frequency determination in GIS environments—New software tool for ArcGIS. *Planetary and Space Science*, *59*(11–12), 1243–1254. https://doi.org/10.1016/j.pss.2010.03.015
Kreslavsky, M. A. (1996). Venus cratering record: Constraints on resurfacing history (pp. 18–22). *Twenty-Seventh Lunar and Planetary Science Conference, Houston, TX*.
Kreslavsky, M. A. (2007). Statistical characterization of spatial distribution of impact craters: Implications to present-day cratering rate on Mars. *Seventh International Conference on Mars, Pasadena, CA*.
Kreslavsky, M. A., Head, J. W., Neumann, G. A., Zuber, M. T., & Smith, D. E. (2014). Kilometer-scale topographic roughness of Mercury: Correlation with geologic features and units. *Geophysical Research Letters*, *41*(23), 8245–8251. https://doi.org/10.1002/2014gl062162
Kreslavsky, M. A., Ivanov, M. A., & Head, J. W. (2015). The resurfacing history of Venus: Constraints from buffered crater densities. *Icarus*, *250*, 438–450. https://doi.org/10.1016/j.icarus.2014.12.024
Marchi, S., Chapman, C. R., Fassett, C. I., Head, J. W., Bottke, W. F., & Strom, R. G. (2013). Global resurfacing of Mercury 4.0–4.1 billion years ago by heavy bombardment and volcanism. *Nature*, *499*(7456), 59–61. https://doi.org/10.1038/nature12280
Michael, G. G., & Neukum, G. (2010). Planetary surface dating from crater size–frequency distribution measurements: Partial resurfacing events and statistical age uncertainty. *Earth and Planetary Science Letters*, *294*(3–4), 223–229. https://doi.org/10.1016/j.epsl.2009.12.041
Michael, G. G., Platz, T., Kneissl, T., & Schmedemann, N. (2012). Planetary surface dating from crater size–frequency distribution measurements: Spatial randomness and clustering. *Icarus*, *218*(1), 169–177. https://doi.org/10.1016/j.icarus.2011.11.033
Miljkovic, K., Wieczorek, M. A., Collins, G. S., Laneuville, M., Neumann, G. A., Melosh, H. J., et al. (2013). Asymmetric distribution of lunar impact basins caused by variations in target properties. *Science*, *342*(6159), 724–726. https://doi.org/10.1126/science.1243224
Minton, D. A., Fassett, C. I., Hirabayashi, M., Howl, B. A., & Richardson, J. E. (2019). The equilibrium size-frequency distribution of small craters reveals the effects of distal ejecta on lunar landscape morphology. *Icarus*, *326*, 63–87. https://doi.org/10.1016/j.icarus.2019.02.021

Neesemann, A., van Gasselt, S., Schmedemann, N., Marchi, S., Walter, S. H. G., Preusker, F., et al. (2019). The various ages of Occator crater, Ceres: Results of a comprehensive synthesis approach. *Icarus*, *320*, 60–82. https://doi.org/10.1016/j.icarus.2018.09.006

Neukum, G., & Ivanov, B. A. (1994). Crater size distributions and impact probabilities on earth from lunar, terrestrial planet, and asteroid cratering data. In T. Gehrels (Ed.), *Hazards due to comets and asterois* (pp. 359–416). Tucson: University Arizona Press.

Neukum, G., Ivanov, B. A., & Hartmann, W. K. (2001). Cratering records in the inner solar system in relation to the lunar reference system. *Space Science Reviews*, *96*, 55–86. https://doi.org/10.1007/978-94-017-1035-0_3

Neukum, G., Oberst, J., Hoffmann, H., Wagner, R., & Ivanov, B. A. (2001). Geologic evolution and cratering history of Mercury. *Planetary and Space Science*, *49*(14–15), 1507–1521. https://doi.org/10.1016/s0032-0633(01)00089-7

Orgel, C., Fassett, C. I., Michael, G., Riedel, C., Bogert, C. H., & Hiesinger, H. (2020). Re-examination of the population, stratigraphy, and sequence of Mercurian basins: Implications for Mercury's early impact history and comparison with the moon. *Journal of Geophysical Research: Planets*, *125*(8). https://doi.org/10.1029/2019je006212

Orgel, C., Michael, G., Fassett, C. I., van der Bogert, C. H., Riedel, C., Kneissl, T., & Hiesinger, H. (2018). Ancient bombardment of the inner solar system: Reinvestigation of the "fingerprints" of different impactor populations on the lunar surface. *Journal of Geophysical Research: Planets*, *123*(3), 748–762. https://doi.org/10.1002/2017je005451

Ostrach, L. R., Robinson, M. S., & Denevi, B. W. (2012). Distribution of impact melt on Mercury and the Moon. *43th Lunar and Planetary Science Conference, The Woodlands, TX, #1113*.

Ostrach, L. R., Robinson, M. S., Whitten, J. L., Fassett, C. I., Strom, R. G., Head, J. W., & Solomon, S. C. (2015). Extent, age, and resurfacing history of the northern smooth plains on Mercury from MESSENGER observations. *Icarus*, *250*, 602–622. https://doi.org/10.1016/j.icarus.2014.11.010

O'Rourke, J. G., Wolf, A. S., & Ehlmann, B. L. (2014). Venus: Interpreting the spatial distribution of volcanically modified craters. *Geophysical Research Letters*, *41*(23), 8252–8260. https://doi.org/10.1002/2014gl062121

Phillips, R. J., Raubertas, R. F., Arvidson, R. E., Sarkar, I. C., Herrick, R. R., Izenberg, N., & Grimm, R. E. (1992). Impact craters and Venus resurfacing history. *Journal of Geophysical Research*, *97*(E10), 15923. https://doi.org/10.1029/92je01696

Povilaitis, R. Z., Robinson, M. S., van der Bogert, C. H., Hiesinger, H., Meyer, H. M., & Ostrach, L. R. (2018). Crater density differences: Exploring regional resurfacing, secondary crater populations, and crater saturation equilibrium on the Moon. *Planetary and Space Science*, *162*, 41–51. https://doi.org/10.1016/j.pss.2017.05.006

Price, M., & Suppe, J. (1995). Constraints on the resurfacing history of Venus from the hypsometry and distribution of volcanism, tectonism, and impact craters. *Earth, Moon, and Planets*, *71*(1–2), 99–145. https://doi.org/10.1007/bf00612873

Prockter, L. M., Ernst, C. M., Denevi, B. W., Chapman, C. R., Head, J. W., Fassett, C. I., et al. (2010). Evidence for young volcanism on Mercury from the third MESSENGER flyby. *Science*, *329*(5992), 668–671. https://doi.org/10.1126/science.1188186

Richardson, J. E. (2009). Cratering saturation and equilibrium: A new model looks at an old problem. *Icarus*, *204*(2), 697–715. https://doi.org/10.1016/j.icarus.2009.07.029

Riedel, C., Michael, G., Kneissl, T., Orgel, C., Hiesinger, H., & van der Bogert, C. H. (2018). A new tool to account for crater obliteration effects in crater size-frequency distribution measurements. *Earth and Space Science*, *5*(6), 258–267. https://doi.org/10.1002/2018ea000383

Riedel, C., Minton, D. A., Michael, G., Orgel, C., Bogert, C. H., & Hiesinger, H. (2020). Degradation of small simple and large complex lunar craters: Not a simple scale dependence. *Journal of Geophysical Research: Planets*, *125*(4). https://doi.org/10.1029/2019je006273

Robbins, S. J. (2019). A new global database of lunar impact craters >1–2 km: 1. Crater locations and sizes, comparisons with published databases, and global analysis. *Journal of Geophysical Research: Planets*, *124*(4), 871–892. https://doi.org/10.1029/2018je005592

Romeo, I. (2013). Monte Carlo models of the interaction between impact cratering and volcanic resurfacing on Venus: The effect of the Beta-Atla-Themis anomaly. *Planetary and Space Science*, *87*, 157–172. https://doi.org/10.1016/j.pss.2013.07.010

Romeo, I., & Turcotte, D. L. (2009). The frequency-area distribution of volcanic units on Venus: Implications for planetary resurfacing. *Icarus*, *203*(1), 13–19. https://doi.org/10.1016/j.icarus.2009.03.036

Schaber, G. G., Strom, R. G., & Kirk, R. L. (1995). *Update on the USGS crater database for Venus, LPSC XXVI, part 3* (pp. 1227–1228). Houston: Lunar and Planetary Institute.

Schaber, G. G., Strom, R. G., Moore, H. J., Soderblom, L. A., Kirk, R. L., Chadwick, D. J., et al. (1992). Geology and distribution of impact craters on Venus: What are they telling us? *Journal of Geophysical Research*, *97*(E8), 13257. https://doi.org/10.1029/92je01246

Snyder, J. P. (1987). Map projections—A working manual. Washington, DC: U.S. Government Printing Office. *U.S. Geological Survey Professional Paper 1395*.

Soderblom, L. A. (1970). A model for small-impact erosion applied to the lunar surface. *Journal of Geophysical Research*, *75*(14), 2655–2661. https://doi.org/10.1029/jb075i014p02655

Sood, R., Chappaz, L., Melosh, H. J., Howell, K. C., Milbury, C., Blair, D. M., & Zuber, M. T. (2017). Detection and characterization of buried lunar craters with GRAIL data. *Icarus*, *289*, 157–172. https://doi.org/10.1016/j.icarus.2017.02.013

Squyres, S., Howell, C., Liu, M., & Lissauer, J. (1997). Investigation of crater "saturation" using spatial statistics. *Icarus*, *125*(1), 67–82. https://doi.org/10.1006/icar.1996.5560

Stöffler, D., Ryder, G., Ivanov, B. A., Artemieva, N. A., Cintala, M. J., & Grieve, R. A. F. (2006). Cratering history and lunar chronology. *Reviews in Mineralogy and Geochemistry*, *60*(1), 519–596. https://doi.org/10.2138/rmg.2006.60.05

Strom, R. G. (1977). Origin and relative age of lunar and Mercurian intercrater plains. *Physics of the Earth and Planetary Interiors*, *15*(2–3), 156–172. https://doi.org/10.1016/0031-9201(77)90028-0

Strom, R. G. (2005). The origin of planetary impactors in the inner solar system. *Science*, *309*(5742), 1847–1850. https://doi.org/10.1126/science.1113544

Strom, R. G., Banks, M. E., Chapman, C. R., Fassett, C. I., Forde, J. A., Head, J. W., III, et al. (2011). Mercury crater statistics from MESSENGER flybys: Implications for stratigraphy and resurfacing history. *Planetary and Space Science*, *59*(15), 1960–1967. https://doi.org/10.1016/j.pss.2011.03.018

Strom, R. G., Schaber, G. G., & Dawson, D. D. (1994). The global resurfacing of Venus. *Journal of Geophysical Research*, *99*(E5), 10899. https://doi.org/10.1029/94je00388

Strom, R. G., Trask, N. J., & Guest, J. E. (1975). Tectonism and volcanism on Mercury. *Journal of Geophysical Research*, *80*(17), 2478–2507. https://doi.org/10.1029/jb080i017p02478

Thomas, R. J., Rothery, D. A., Conway, S. J., & Anand, M. (2014). Long-lived explosive volcanism on Mercury. *Geophysical Research Letters*, *41*(17), 6084–6092. https://doi.org/10.1002/2014gl061224

Thomson, B. J., Grosfils, E. B., Bussey, D. B. J., & Spudis, P. D. (2009). A new technique for estimating the thickness of mare basalts in Imbrium Basin. *Geophysical Research Letters*, *36*(12). https://doi.org/10.1029/2009gl037600

Turcotte, D. L., Morein, G., Roberts, D., & Malamud, B. D. (1999). Catastrophic resurfacing and episodic subduction on Venus. *Icarus*, *139*(1), 49–54. https://doi.org/10.1006/icar.1999.6084

Virtanen, P., Gommers, R., Oliphant, T. E., Haberland, M., Reddy, T., Cournapeau, D., et al. (2020). SciPy 1.0: Fundamental algorithms for scientific computing in Python. *Nature Methods*, *17*(3), 261–272. https://doi.org/10.1038/s41592-019-0686-2

Watters, T. R., Daud, K., Banks, M. E., Selvans, M. M., Chapman, C. R., & Ernst, C. M. (2016). Recent tectonic activity on Mercury revealed by small thrust fault scarps. *Nature Geoscience*, *9*(10), 743–747. https://doi.org/10.1038/ngeo2814

Watters, T. R., Head, J. W., Solomon, S. C., Robinson, M., Chapman, C. R., Denevi, B. W., et al. (2009). Evolution of the rembrandt impact basin on Mercury. *Science*, *324*(5927), 618–621. https://doi.org/10.1126/science.1172109

Whitten, J., Head, J. W., Staid, M., Pieters, C. M., Mustard, J., Clark, R., et al. (2011). Lunar mare deposits associated with the Orientale impact basin: New insights into mineralogy, history, mode of emplacement, and relation to Orientale Basin evolution from Moon Mineralogy Mapper (M3) data from Chandrayaan-1. *Journal of Geophysical Research*, *116*. https://doi.org/10.1029/2010je003736

Wieczorek, M. A., Neumann, G. A., Nimmo, F., Kiefer, W. S., Taylor, G. J., Melosh, H. J., et al. (2012). The crust of the Moon as seen by GRAIL. *Science*, *339*(6120), 671–675. https://doi.org/10.1126/science.1231530

Wilhelms, D. E. (1976). Mercurian volcanism questioned. *Icarus*, *28*(4), 551–558. https://doi.org/10.1016/0019-1035(76)90128-7

Wilhelms, D. E. (1987). *The geologic history of the Moon* (p. 302): U. S. Geological Survey Professional Paper 1348.

Williams, K. K., & Zuber, M. T. (1998). Measurement and analysis of lunar basin depths from clementine altimetry. *Icarus*, *131*(1), 107–122. https://doi.org/10.1006/icar.1997.5856

Wilson, L., & Head, J. W. (2008). Volcanism on Mercury: A new model for the history of magma ascent and eruption. *Geophysical Research Letters*, *35*(23). https://doi.org/10.1029/2008gl035620

Woronow, A. (1977). Crater saturation and equilibrium—A Monte Carlo simulation. *Journal of Geophysical Research*, *82*, 2447–2456. https://doi.org/10.1029/JB082i017p02447

Zhu, M., Wünnemann, K., Potter, R. W. K., Kleine, T., & Morbidelli, A. (2019). Are the Moon's nearside-farside asymmetries the result of a giant impact? *Journal of Geophysical Research: Planets*, *124*(8), 2117–2140. https://doi.org/10.1029/2018je005826

Zuber, M. T., Smith, D. E., Phillips, R. J., Solomon, S. C., Neumann, G. A., Hauck, S. A., et al. (2012). Topography of the northern hemisphere of Mercury from MESSENGER laser altimetry. *Science*, *336*(6078), 217–220. https://doi.org/10.1126/science.1218805